

3D Object Detection for Autonomous Driving: A Survey

Rui Qian, Xin Lai, and Xirong Li
Renmin University of China
Beijing, China
{rui-qian, laixin, xirong}@ruc.edu.cn

Abstract—Autonomous driving is regarded as one of the most promising remedies to shield human beings from severe crashes. To this end, 3D object detection serves as the core basis of such perception system especially for the sake of path planning, motion prediction, collision avoidance, etc. Generally, stereo/monocular images with corresponding 3D point clouds are already standard layout for 3D object detection, out of which point clouds are increasingly prevalent with accurate depth information being provided. Despite existing efforts, 3D object detection on point clouds is still in its infancy due to high sparseness and irregularity of point clouds by nature, misalignment view between camera view and LiDAR bird’s eye of view for modality synergies, occlusions and scale variations at long distances, etc. Recently, profound progress has been made in 3D object detection, with a large body of literature being investigated to address this vision task. As such, we present a comprehensive review of the latest progress in this field covering all the main topics including sensors, fundamentals, and the recent state-of-the-art detection methods with their pros and cons. Furthermore, we introduce metrics and provide quantitative comparisons on popular public datasets. The avenues for future work are going to be judiciously identified after an in-deep analysis of the surveyed works. Finally, we conclude this paper.

Index Terms—3D object detection, Autonomous driving, Point clouds

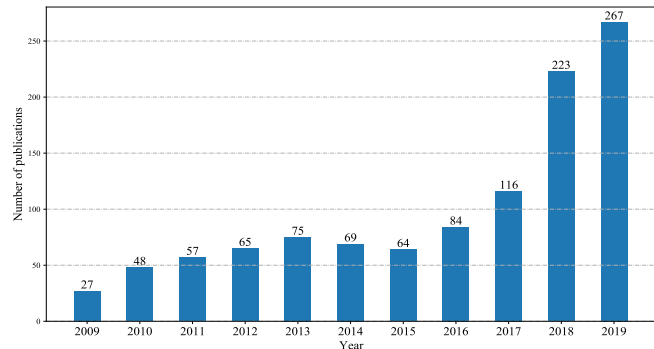
I. INTRODUCTION

WHY is autonomous driving? The rise of Autonomous Driving (AD) is sure to benefit the whole society from the following aspects: 1) Safety. The paramount aim for AD is to address the problem of safety. According to National Highway Traffic Safety Administration (NHTSA) [1, 2], about 36,560 people died in the U.S. in 2018, as a consequence of motor vehicle-related crashes. What’s more, 94% of severe crashes are owe to human error. The continuing evolution of AD is poised to save lives and change the car insurance industry in essence. 2) Economic benefits. A NHTSA study reveals \$242 billion is spent on motor vehicle crashes in 2010, involved in disentangling traffic accidents and treating the wounded. 3) Efficiency and convenience. With AD system, traffic flow could be smoothed with the help of big data, the time for daily commutes can be radically reduced. 4) Mobility. Autonomous vehicles will provide new mobility options, creating new employment opportunities for people with disabilities. More details can be found in [1–3].

X. Lai contributes equally to this work and should be considered as co-first author. Xirong Li contributes equally to this work and is the corresponding author.

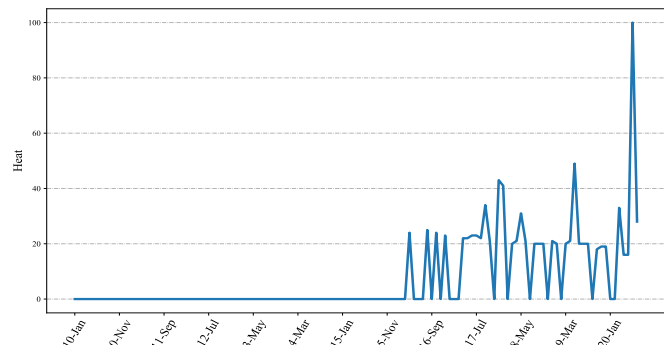
Manuscript received Jun 19, 2021; revised ** **, 2021.

The number of publications in 3D object detection



(a) The increasing number of publications in 3D object detection from 2009 to 2019. (Data from Google scholar advanced search: allintitle: “3D object detection”).

The trend of heat change with time



(b) The trend of heat change with time from 2010 to 2020. (Data from Google trends by searching key word: “3d object detection autonomous driving”).

Fig. 1: The increasing number of publications from 2009 to 2019 and the heat trends from January 2010 to June 2020. Note that 3D object detection is getting its popularity.

What is autonomous driving? Universally acknowledged, 5 levels exist at present. The biggest demarcation of AD happens at Level 3, with completely certain safety-critical functions being shifted to the vehicle under certain traffic conditions.

Level 0: The driver (human) does all the driving: steering, brakes, and power, etc.

Level 1: An advanced driver assistance system (ADAS) automatically assists the human driver with specific and limited functions, (e.g., steering or braking). Note that the driver still controls almost all the behaviours.

Level 2: In level 2, the driver assistance system actually

controls both steering and acceleration/deceleration under certain circumstances. Full human attention is still needed in case of emergency.

Level 3: Drivers are still indispensable to intervene if necessary, but are able to shift all the functions to the vehicle.

Level 4: This is so called “fully autonomous”. Vehicles perform all driving functions, which is limited to the “operational design domain (ODD)” for an entire trip.

Level 5: A fully-autonomous system is expected to function as good as a human driver, coping with various unconstrained driving scenarios. The occupants of the vehicles are just passengers in the foreseeable future.

What is 3D object detection? 3D object detection is to detect physical objects from 3D sensor data, with oriented 3D bounding boxes being estimated and with specific categories being assigned. 3D object detection serves as the core of 3D scene perception and understanding. Thousands of downstream applications, such as autonomous driving, housekeeping robots, and augmented/virtual reality, etc., have sprung up with the availability of various types of 3D sensors [4]. Generally, three types of 3D representations commonly exist, including point clouds 2(a), meshes 2(b), volumetric grids 2(c), out of which point clouds are the preferred representation in many cases. Point clouds neither consume storages as much as meshes that consist of a large number of faces, nor lose original geometric information like volumetric grids due to quantization. Point clouds are close to raw LiDAR sensor data 4.

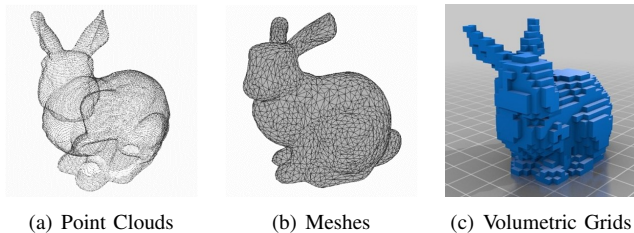


Fig. 2: Three types of commonly existing 3D representations. Image from Qi et al. [5].

3D object detection [6–8] has made remarkable progress, though, it has still trailed its 2D counterpart thus far[9–18]. 3D object detection looks into detecting visual objects of a certain class with accurate geometric, shape and scale information: 3D position, orientation, and occupied volume [19], providing a better understanding of surroundings for machines, and posing a difficult technological challenge simultaneously. It is generally believed that the key to the success of Convolution Neural Networks is the capability of leveraging spatially-local correlations in dense representations [20]. However, directly applying CNNs kernels against point clouds inevitably contributes to desertion of shape information and variance to point ordering [20]. On this basis, this paper carefully analyzes the recently state-of-the-art 3D object detection methods.

Last but not least, it is also important to note that modern autonomous driving system relies heavily on deep learning. Whereas, deep learning methods have already been proved to be vulnerable to forgeries. As such, this poses an inherent

security risk(e.g., sabotage, adverse conditions, and blind spots, etc.) to the automated industry. Ultimately, adversarial attacks with regard to 3D object detection are largely in their infancy [21].

Compared to the existing literature, we summarize our contributions as follows:

- 1) **A survey with new taxonomy which is more fine-grained:** Compared with [6, 7], we dig in further to provide more fine-grained classification on the existing efforts [6, 7] which facilitates readers to grasp the characteristics of each method intuitively and concretely. For instance, point cloud-based methods are meant to be exhaustive, but when we group point cloud-based methods further into multi-view-based, voxel-based, point-based, and point-voxel-based methods on the basis of representation learning, readers should be able to identify the main ideas of point cloud-based methods without effort.
- 2) **A survey with new taxonomy which is more systematic:** As shown in Fig. 2 and Fig. 6, the outbreak happening after 2018 has undergone a profound transition, regardless of social concerns and effectiveness of the method itself. 3D perception system has witnessed a process of continuous self-improvement, which is not really established until high-performance detectors are proposed after 2018, e.g., PointRCNN [22], PV-RCNN [23]. Whereas, literature [7] only covers the progress before 2018. Besides, to the best of our knowledge, only a handful of literature is associated with 3D point clouds, not to mention the far unexplored fields focusing on autonomous driving.
- 3) **A survey with new taxonomy which is more inclusive:** In [8], Guo et al. grouped Part- A^2 [24], PV-RCNN [23], Point-GNN [25] into “Other Methods”, leaving the problem unsolved. Studies [6, 7, 26] have discussed the taxonomy carefully, but when it comes to multimodal fusion, they only introduced the basic concept of early fusion, late fusion, and deep fusion, without identifying which category each method belongs to explicitly. Whereas, we defined two new paradigms to adapt to ongoing changes.
- 4) **A survey with new taxonomy which is a supplementary rather than an alternative:** As opposed to existing survey [8], we specifically focus on 3D object detection in the context of autonomous driving, rather than all related subtopics of 3D point clouds, (e.g., 3D shape classification, 3D point cloud segmentation and tracking, etc.) Given that the limited space available, one can not delve into such details, with all the materials being involved. Instead, we start with quite basic concepts, providing a glimpse of evolution of 3D object detection in terms of autonomous driving under our defined paradigms, together with comprehensive comparisons on publicly available datasets being manifested, with pros and cons being judiciously presented.

The rest of this paper is organized as follows. In Section II, we discuss the commonly used 3D sensors. In Section III,

TABLE I: Advantages and disadvantages of different sensors.

Sensors	Advantages	Disadvantages	Publications
Monocular Camera	<ul style="list-style-type: none"> •cheap and available for multiple situations •informative color and texture attributes 	<ul style="list-style-type: none"> •no depth or range detecting feature •susceptible to weather and light conditions 	[27], [28], [29] [30], [31], [32]
Stereo Camera	<ul style="list-style-type: none"> •depth information provided •informative color and texture attributes •high frame rate 	<ul style="list-style-type: none"> •computationally expensive •sensitive to weather and light conditions •limited Field-of-View(FoV) 	[33], [34], [35]
LiDAR	<ul style="list-style-type: none"> •accurate depth or range detecting feature •less affected by external illumination •360° FoV 	<ul style="list-style-type: none"> •high sparseness and irregularity by nature •no color and texture attributes •expensive and critical deployment 	[22, 23, 36–39], [25] [40], [41], [42, 43] [44, 45], [24, 46, 47]
Solid State LiDAR	<ul style="list-style-type: none"> •more reliable compared with surround view sensors •cost decrease 	<ul style="list-style-type: none"> •error increase when different points of view are merged in real time •Still under development and limited FoV 	- -

we introduce basic concepts and notations. In Section IV, we review the latest existing state-of-the-art 3D object detection methods with their corresponding pros and cons in the context of autonomous driving. Commonly used metrics, comprehensive comparisons of the state-of-the-arts, and publicly available datasets are summarized in Section V. Afterwards, we identify future research directions. In Section VI, we conclude this paper.

II. SENSORS

We human beings leverage visual and auditory systems to perceive the real world when driving, so how about autonomous vehicles? If they were to drive like a human, then to identify what they see on the road constantly is the way to go. To this end, sensors matter. It is sensors that empower vehicles a series of abilities: obstacles perception, overtaking, automatic emergency braking, collision avoidance, ride-hailing, traffic light and pedestrian detection, etc. In general, the most commonly used sensors can be divided into two categories: passive sensors and active sensors. The on going debate among industry experts is whether or not to just equip vehicles with camera systems (no LiDAR), or deploy LiDAR together with on-board camera systems. Currently, Waymo, Uber and Velodyne are in support of LiDAR, while Tesla has been outnumbered, in favor of camera systems. Given that camera is considered to be one of the typical representatives of passive sensors, and LiDAR is regarded as a representative of active sensors, we first introduce the basic concepts of passive sensors and active sensors, then take camera and LiDAR as an example to discuss how they serve the autonomous driving system, together with pros and cons being manifested in table II.

A. Passive Sensors

Passive sensors are anticipated to receive natural emissions emanating from both the Earth’s surface and its atmosphere. These natural emissions could be natural light or infrared rays. For instance, a camera directly grabs a bunch of color points from the optics in the lens and arranges them into an image array that is often referred to as a digital signal for scene understanding. Inspired by recent advancements in computer vision algorithms to analyze over image signals, 2D/3D object

detection has undergone profound progress. So far Tesla has been successfully leveraging camera systems (no LiDAR) to obtain a 360 degree view for its autonomous vehicles (as of this main text in June 2021). Primarily, a monocular camera lends itself well to informative color and texture attributes, better visual recognition of text from road signs, and high frame rate at a negligible cost, etc. Whereas, it is lack of depth information, which is crucial for accurate position estimation in the real world. To overcome this, a stereo camera uses matching algorithms to align correspondences in both left and right images for depth recovery. While cameras have shown potentials as a reliable visioning system, it is hardly sufficient as a standalone system. Specifically, a camera is prone to degrade its accuracy in cases where luminosity is low at night-time or rainy weather conditions occur. As a consequence, Tesla has to use auxiliary sensors to fall-back onto in case that camera system should malfunction or disconnect.

B. Active Sensors

Active sensors are expected to measure reflected signals that are transmitted by the sensor, which are bounced by the Earth’s surface or its atmosphere. Typically, LiDAR (Light Detection And Ranging) is a point-and-shoot device with three basic components of len, laser and detector, which spits out light pulses that will bounce off the surroundings in the form of 3D points, referred to as “point clouds”. High sparseness and irregularity by nature and the absence of texture attributes are the primary characteristics of a point cloud, which is well distinguished from image array. Since we have already known how fast light travels, the distance of obstacles could be determined without effort. LiDAR system emits thousands of pulses that spin around in a circle per second, with a 360 degree view of surroundings for the vehicles being provided. For example, Velodyne HDL-64L produces 120 thousand points per frame with a 10 Hz frame rate. Obviously, LiDAR is less affected by external illumination conditions (e.g., at night-time), given that it emits light pulses by itself. Although LiDAR system has been hailed for high accuracy and reliability compared with camera system, it does not always hold true. Specifically, wavelength stability of LiDAR is susceptible to variations in temperature, while adverse weather (e.g., snow or fog) is prone to result in poor SNR (Signal-to-Noise Ratio) in the

LiDAR’s detector. Another issue with LiDAR is the high cost of deployment. A conservative estimate according to Velodyne, so far, is about \$70,000 [7]. In the foreseeable future of LiDAR, how to decrease cost and how to increase resolution and range are where the whole community is to march ahead. As for the former, the advent of Solid State LiDAR is expected to address this problem of cost decrease, with the help of several stationary lasers that emit light pulses along a fixed field of view. As for the latter, the newly announced Velodyne VLS-128 featuring 128 laser pulses and 300m radius range has been on sale, which is going to significantly facilitate better recognition and tracking in terms of public safety.

C. Discussion

Fatalities occurred with autonomous vehicles have already increased the society’s grave concern about safety. If autonomous vehicles were to hit the road legally, they at least need to satisfy three basic characteristics: high accuracy, high certainty, and high reliability. To this end, sensor fusion incorporating the merits of two worlds (camera vs LiDAR) is going to be necessary. From a sensor standpoint, LiDAR provide depth information close to linearity error with a high level of accuracy, but it is susceptible to adverse weather (e.g., snow or fog). Camera is intuitively much better at visual recognition in cases where color or texture attributes are available (see Fig. 16), but they are not sufficient as a standalone system as aforementioned. Note that certainty is still an important yet largely unexplored problem. A combination of LiDAR and camera is anticipated to ensure detection accuracy and improve prediction certainty. With regard to reliability, two facets should be considered: sensor calibration and system redundancy. Sensor calibration undoubtedly increases the difficulty of deployment and directly affects the reliability of the whole system. Studies [48–50] have looked into calibrating sensors to avoid drift over time. System redundancy is to have a secondary sensor to fall-back onto in case of a malfunction or outage. The community should be keenly aware of the safety risk of over-reliance on a single sensor. More details will be discussed in Section IV-C.

III. FUNDAMENTALS

In this section, we formulate 3D object detection problem, list commonly used notations, and introduce basic coordinate transformation.

A. Problem Formulation

Unless otherwise stated, notations used in this survey are manifested in Table II. Given that all the methods associated bellow are based on KITTI dataset for comparisons, we follow the camera coordinate system adopted by the project of Karlsruhe Institute of Technology and Toyota Technological Institute (KITTI) [19, 51] in the remainder of main text: it is a right-handed coordinate system, when x -axis points to right, y -axis points down with regard to the 2D image plane, z -axis stands for depth and is perpendicular to the 2D image plane. Denote by $\{\{\mathcal{B}_i, \mathcal{C}_i\} = \Phi(\mathcal{D}_i; \Theta) : i = 1, \dots, M\}$

TABLE II: Commonly used notations.

Notations	Descriptions
$ \cdot $	The length of a set.
$\mathcal{B} \in \mathbb{R}^9$	A 3D bounding box.
$\Phi(\mathcal{D}; \Theta)$	Models with learnable parameters Θ .
$\mathcal{P} \in \mathbb{R}^{n \times 4}$	A point cloud with coordinates p and reflectance r .
\mathcal{K}	The maximum kept voxels for a point cloud.
\mathcal{T}	The occupancy of a voxel.
\mathcal{N}	The number of points within a point cloud.
$\mathbf{T}_{velo}^{cam} \in \mathbb{R}^{3 \times 4}$	The rigid body transformation matrix.
$\mathbf{R}_{rect}^{(0)} \in \mathbb{R}^{3 \times 3}$	The rectifying rotation matrix.
$\mathbf{P}_{rect}^{(i)} \in \mathbb{R}^{3 \times 4}$	Projection matrix after rectification of i th camera.
$\mathbf{K}_{rect}^{(i)}$	The intrinsics of i th camera.
$[\cdot]$	The floor function.
$\mathcal{D} \subseteq \mathbb{R}^{n \times 3}$	The subset of a continuous 3D space.

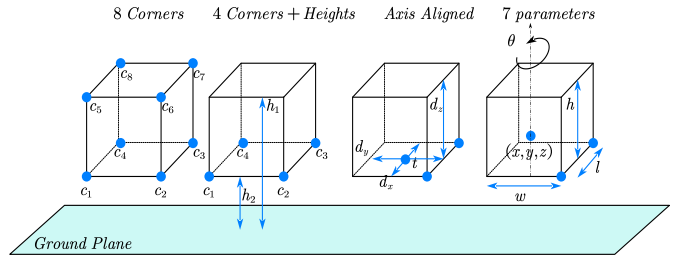


Fig. 3: Comparison of the 3D bounding box parameterization between 8 corners proposed in [52], 4 corners with heights proposed in [53], the axis aligned box encoding proposed in [54], and the 7 parameters for an oriented 3D bounding box adopted in [22, 32, 41, 43, 45].

M detected 3D bounding boxes through model, $\Phi(\mathcal{D}; \Theta)$ that is specified in the following Section IV. Note that $\mathcal{B} = \{[w_i, h_i, l_i, x_i, y_i, z_i, \theta_i, \phi_i, \psi_i] \in \mathbb{R}^9 : i = 1, \dots, M\}$, set \mathcal{C} is the interested categories, and $\mathcal{D} \subseteq \mathbb{R}^{n \times 3}$ is a subset of continuous 3D space. Besides, w_i, h_i, l_i represent width, height, length respectively, and x_i, y_i, z_i are the 3D coordinates of the bottom center of \mathcal{B} . As for the rotation angle, only θ_i is considered assuming all the objects are on the ground [31]. As shown in Fig. 3, 3D bounding box is commonly encoded as a set of seven parameters, including 3D center coordinates (x, y, z) , apart from size dimensions (w, h, l) , and its corresponding heading angle θ . Such a parameterization is widely accepted by most previous works [22, 32, 41, 43, 45]. Furthermore, Fig. 4 illustrates an overview of 3D object detection from point clouds.

B. Coordinate Transformation

Whether it is multimodal fusion-based or point cloud-based methods, coordinate transformation runs through from beginning to end. We do not intend to involve that much specific mathematical derivation which is beyond the scope of



Fig. 4: An overview of 3D object detection from point clouds. 3D object detection is to detect physical objects from 3D sensor data, with oriented 3D bounding boxes being estimated and with specific categories being assigned. Note that Fig. 4 are in LiDAR coordinates.

this survey, but it is necessary to give its basic concepts given that it is indeed an essential prerequisite of preprocessing (e.g., data augmentation). Since most of the existing researches are based on KITTI dataset, we will take KITTI dataset as an example to introduce the main principles which holds true for its counterparts. In general, LiDAR and camera coordinate systems are defined as: 1) LiDAR coordinates: x =forward, y =left, z =up. 2) Camera coordinates: x =right, y =down, z =forward.

Given a 3D point $\mathbf{p} = (x, y, z, 1)^T$ in LiDAR coordinates, its corresponding point $\mathbf{y} = (u, v, 1)^T$ in the i -th camera image is given as:

$$\mathbf{y} = \mathbf{P}_{rect}^{(i)} \mathbf{R}_{rect}^{(0)} \mathbf{T}_{velo}^{cam} \mathbf{p}, \quad (1)$$

where $i \in \{0, 1, 2, 3\}$ is the camera index in the KITTI sensor setups, out of which camera 0 is the reference coordinates. $\mathbf{T}_{velo}^{cam} \in \mathbb{R}^{3 \times 4}$ is the rigid body transformation from LiDAR coordinates to camera coordinates, $\mathbf{R}_{rect}^{(0)} \in \mathbb{R}^{3 \times 3}$ is the rectifying rotation matrix, and $\mathbf{P}_{rect}^{(i)} \in \mathbb{R}^{3 \times 4}$ is projection matrix after rectification. Note that all four camera centers are aligned to the same x/y -plane. In particular,

$$\mathbf{P}_{rect}^{(i)} = \begin{pmatrix} f_u^{(i)} & 0 & c_u^{(i)} & -f_u^{(i)} b_x^{(i)} \\ 0 & f_v^{(i)} & c_v^{(i)} & 0 \\ 0 & 0 & 1 & 0 \end{pmatrix}, \quad (2)$$

with

$$\mathbf{K}_{rect}^{(i)} = \begin{pmatrix} f_u^{(i)} & 0 & c_u^{(i)} \\ 0 & f_v^{(i)} & c_v^{(i)} \\ 0 & 0 & 1 \end{pmatrix}. \quad (3)$$

here, $b_x^{(i)}$ is the baseline with respect to reference camera 0, $f_u^{(i)}$ and $f_v^{(i)}$ denote camera focal length from u -axis and v -axis in camera coordinates respectively. In fact, $\mathbf{K}_{rect}^{(i)}$ denotes camera intrinsics. We refer readers to [19, 51] for more details.

IV. 3D OBJECT DETECTION METHODS

2D object detection has a catalytic effect in spurring progress in 3D object detection somewhat. As shown in Fig. 6, 3D object detection methods can be categorized into monocular/stereo image-based IV-A, point cloud-based IV-B and multimodal fusion-based methods IV-C in terms of the modality of input data. Note that point cloud-based methods which predominate in 3D object detection, can further be classified into multi-view-based, voxel-based, point-based, and point-voxel-based methods on the basis of representation learning. Multimodal fusion-based methods have been getting popularity nowadays, but it is no-trivial to exploit the synergies of different domains (i.e., images and point clouds). To explicitly distinguish diverse multimodal fusion-based methods,

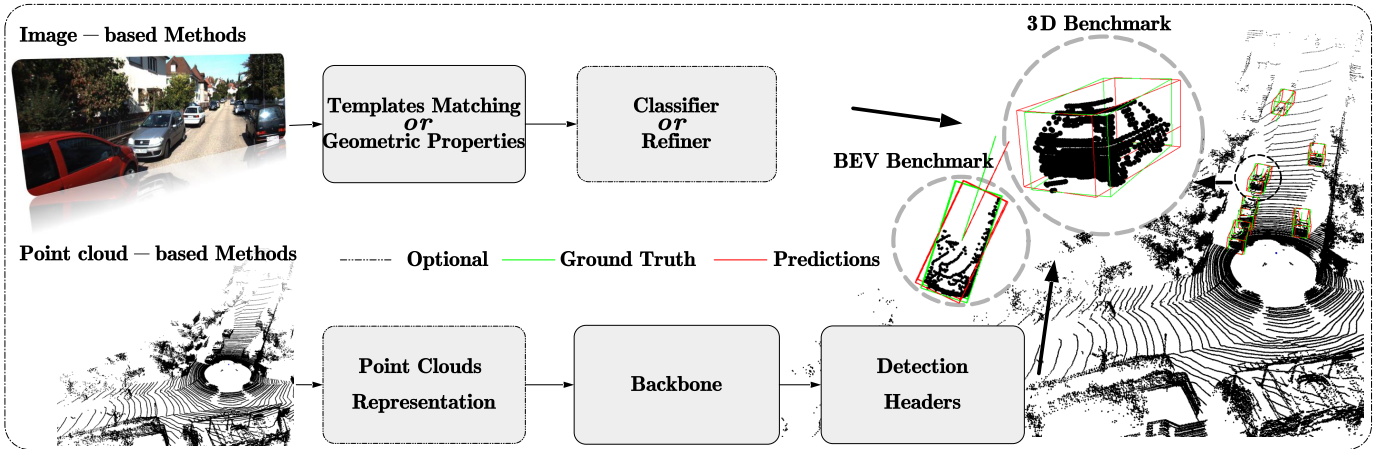


Fig. 5: Pipeline of 3D Object Detection in General. Generally, image-based methods either exploit carefully manual feature engineering to exhaustively search templates via machine learning (e.g., SVM) [27, 28, 35, 55] or leverage considerable domain expertise to roughly estimate 3D pose via geometric properties from empirical observation, with high-quality 2D bounding boxes being provided via the off-the-shelf 2D detectors [29, 31, 33]. Nevertheless, standard point cloud-based methods commonly consists of three components: 1) Point cloud representation; 2) Backbone, 3) Detection headers. Given exceptions [22, 25, 39] directly take raw point clouds as input leaving feature learning implicitly, we use dotted line to reveal optional operation. In a sequel, on the basis of image-based and point cloud-based methods, multimodal fusion-based methods have become even thriving, with numerous literature being proposed [52, 56–58].

we define two new categories of fusion strategies: sequential fusion-based methods and parallel fusion-based methods. We introduce monocular/stereo image-based methods, point cloud-based methods, and multimodal fusion-based methods in line with the chronological order in which each method emerges. We put multimodal fusion-based methods at last since it’s on the basis of the others. Now, we analyze each category individually in deep in the following subsections.

A. Monocular/Stereo Image-based Methods

These methods which are the most similar stream in spirit to 2D object detection among those in 3D, only take monocular/stereo images as input to predict 3D object instances. Generally two lines exist: **Templates Matching based Methods** and **Geometric Properties based Methods**. As for the former, region proposals are the essential ingredients of this line. In fact, how to propose high-quality regions where objectness may exist in 2D object detection has been extensively studied [59], varying from traditional hand-crafted grouping (e.g., SelectiveSearch [60]) and window scoring (e.g., EdgeBoxes [61]) methods to recently Region Proposal Network (RPN) [13] accompanying with the success of CNNs. Methods to obtain region proposals are meant to be exhaustive. Nevertheless, the purpose of extracting regional coresponding priors (i.e., segmentation, shape, and free space, etc.) of images to exhaustively score and match 3D representative templates is always with consistency [27, 28, 35, 55]. Whereas, the later can be reduced to the perspective n-point problem (PnP) [62] to roughly estimate 3D pose via geometric properties from empirical observation, with high-quality 2D bounding boxes being provided via the off-the-shelf 2D detectors [11–18]. Recently, inspired by the encouraging success of point cloud-based methods, another attempt occurs by reprojecting image

coordinates back into 3D space via computing disparity to mimic LiDAR signal (hereafter called pseudo LiDAR), and then resorts to high-performance point cloud-based methods. We name it **Pseudo LiDAR based Methods**.

Templates Matching based Methods. These methods are prone to perform 2D/3D matching via exhaustively sampling and scoring 3D proposals as representative templates.

Templates matching based methods are typically exemplified by the early and well known 3DOP [55] proposed by Chen et al., which consumes a stereo image pair as input to estimate depth and compute a point cloud via reprojecting pixel-wise coordinates in the image plane back into 3D space. 3DOP formulates the problem of proposal generation as energy minimization of a Markov Random Field (MRF) with respect to carefully designed potentials (e.g., object size priors, ground plane, and point cloud density, etc.). With a diverse set of 3D object proposals being obtained, 3DOP resorts Fast R-CNN [11] pipeline to jointly regress object locations. Subsequently, on the possible occasions when cars are only equipped with a single camera, Chen et al. proposed Mono3D [27] to achieve on par performance through using a monocular camera only instead of stereo one. Different from 3DOP, Mono3D directly samples 3D object candidates from 3D space through the usage of sliding windows without computing depth information, assuming the ground plane where objects lies should be orthogonal to the image plane to reduce search efforts. Potentials, for instance, semantic segmentation, instance level segmentation as well as location priors are exploited to exhaustively score candidates in the image plane to select the most promising one before conducting detections via Fast R-CNN [11] pipeline specified in 3DOP [55]. Either 3DOP [55] or Mono3D [27] outputs class-specific proposals, which means potentials needs to be newly designed for each category

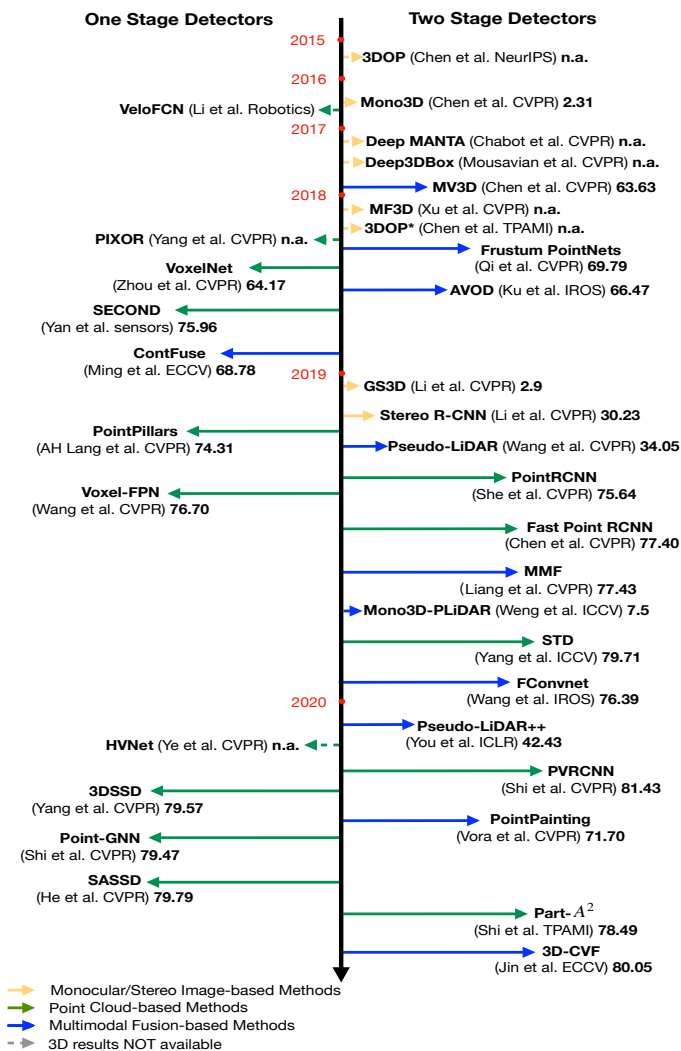


Fig. 6: Chronological axis of 3D object detection. Detectors in this figure: 3DOP [35, 55], Mono3D [27], Deep MANTA [28], Deep3DBox[29], GS3D [31], Stereo R-CNN [33], MF3D [30], Mono3D-PLiDAR [32], VeloFCN [36], PIXOR [37], VoxelNet [45], SECOND [41], PointPillars [43], Voxel-FPN [44], Part-A² [24], HVNet [47], PointRCNN [22], 3DSSD [39], Point-GNN [25], Fast Point R-CNN [63], STD [38], PV-RCNN [23], SA-SSD [40], Frustum PointNets [56], F-ConvNet [46], PointPainting [57], Pseudo-LiDAR [64], Pseudo-LiDAR++ [65], MV3D [52], AVOD [53], ContFuse [58], MMF [66], 3D-CVF [67].

separately. Nevertheless, over-reliance on careful engineering and considerable domain expertise limit the generalizability of these models for complex scenarios. Another attempt is seen in Deep MANTA [28] proposed by Chabot et al., which utilizes a customized 2D detector to output 2D bounding boxes, associated with 2D part coordinates, part visibility and 3D template similarity supervised by a large CAD database of 3D models. With the best corresponding 3D template being chosen from a template database according to the predicted 3D template similarity, 2D/3D matching in [68] is conducted to recover 3D geometry. The drawbacks are: Deep MANTA needs to maintain a huge CAD database of 3D models which

is ill-suited to be generalized to the category which is absent from the database.

Geometric Properties based Methods. Instead of requiring extensive proposals to achieve high recall, these methods start with accurate 2D bounding boxes directly to roughly estimate 3D pose from geometric properties obtained by empirical observation.

Mousavian et al. proposed Deep3DBox[29], leveraging the geometric properties that the perspective projection of 3D corners should tightly touch at least one side of the 2D bounding box. Li et al. proposed GS3D [31], which detects complete 3D instances via monocular RGB image only, without extra data or label being introduced. Specifically, GS3D adds an extra branch of orientation prediction on the basis of the Faster RCNN [13] framework to predict reliable 2D bounding boxes and observation orientations, referred to as 2D+O subnet. Then GS3D obtains coarse 3D boxes, referred to as guidances, based on the empirical evidence in the context of autonomous driving, that the 3D box top center is approximately close to the top midpoint of its corresponding 2D bounding box. Last, features extracted from both 2D box and three visible surfaces of 3D box are fused to eliminate the problem of representation ambiguity before fed into 3D subnet for further refinement. Although GS3D shows a significant performance gain over existing monocular image-based methods, GS3D depends upon the empirical knowledge, which is inaccurate and vulnerable to the ranges and sizes of the objects. Another example of utilizing projection relationships between 2D and 3D is Stereo R-CNN [33]. Li et al. proposed Stereo R-CNN [33], which fully exploits semantic properties as well as dense constraints in stereo imagery. In particular, Stereo R-CNN adopts weight-share network, namely ResNet-101 [69] and FPN [70] as backbone, to extract both left and right image features respectively, then a Region of Interest (RoI) alignment operation is applied, with corresponding RoI proposals being cropped. Next, these selected RoI features are fused via concatenation before fed into a stereo regression branch. Simultaneously, four semantic keypoints are predicted by mimicking Mask R-CNN [18], with RoI features of left branch being utilized. Last, the 3D box estimation can be artfully addressed resorting to geometric constraints, that is, the projection relationships between 3D corners and 2D boxes as well as the predicted keypoints.

Pseudo LiDAR based Methods. These methods first perform depth estimation and then resort to existing point cloud-based methods.

Xu et al. proposed MF3D [30], which performs multi-level fusion for image features and pseudo LiDAR. Specifically, MF3D first computes the disparity via a stand-alone monocular depth estimation module to obtain a pseudo LiDAR. Simultaneously, a standard 2D region proposal network is employed taking as input RGB images fused with the converted front view (see algorithm 3) features obtained by the disparity map. With 2D region proposals being obtained, features both from RGB images and pseudo LiDAR are fused by concatenation for further refinement. Recently, Weng et al. proposed Mono3D-PLiDAR [32], which lifts the input image into 3D camera coordinates, namely, pseudo-LiDAR points,

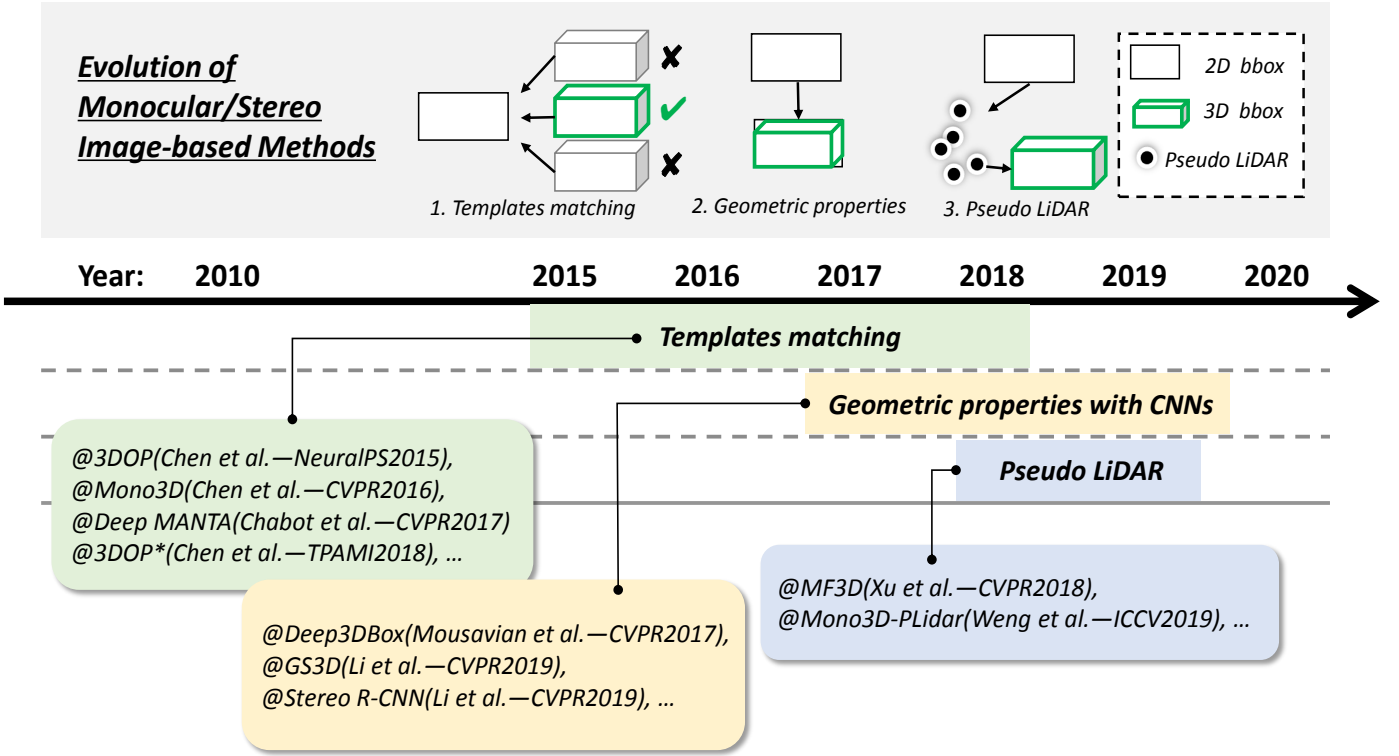


Fig. 7: Evolution of monocular/stereo image-based methods: 1) Templates matching, 2) Geometric properties, 3) Pseudo LiDAR. Detectors in this figure: 3DOP [35, 55], Mono3D [27], Deep MANTA [28], Deep3DBox[29], GS3D [31], Stereo R-CNN [33], MF3D [30], Mono3D-PLidar [32].

via monocular depth estimation (e.g., DORN [71]). Then a 3D object detector, called Frustum PointNets [56] is applied with the pseudo-LiDAR. Weng et al. reveals that Pseudo LiDAR has a large amount of noise due to the error of monocular depth estimation, which reflects in two aspects: a local misalignment w.r.t the LiDAR points and a problem of depth artifacts. To overcome the former, Mono3D-PLiDAR uses a 2D-3D bounding box consistency loss (BBCL) to supervise the training. To alleviate the latter, Mono3D-PLiDAR adopts the instance mask predicted by Mask-RCNN [18] instead of the 2D bounding box to reduce irrelevant points within frustum. We refer the interested reader to Fig. 15(f) for details of frustum architecture. Pseudo LiDAR based methods indeed obtain a promising performance gain in accuracy, which somehow provide enlightenments for exploring the synergies of two modalities, that is, images and point clouds.

In summary 7, monocular/stereo image-based methods have their pros and cons. These methods take images only as inputs, which provide color attributes as well as texture information. Typically, they rely on a considerable amount of domain expertise to design vector representation. As the absence of depth information, one possible remedy is to investigate depth estimation algorithm. For an autonomous system, redundancy is indispensable to guarantee safety apart from economic concerns, so image-based methods are poised to make a continuing impact over the next few years.

B. Point Cloud-based Methods

The essence of CNNs is sparse interaction and weight sharing, whose kernels have been proved to be effective in exploiting spatially-local correlations in regular domains [20], that is, euclidean structure, by a weighted sum of center pixel and its adjacent pixels. Whereas, CNNs is ill-suited in cases where data is represented in irregular domains, (e.g., social networks, point clouds, etc.). Since a point cloud is irregular and unordered, directly convolving against it suffers from “desertion of shape information and variance to point ordering” [20], as Li et al. notes. As shown in Fig. 8, suppose set $\mathcal{F} = \{f_i \in \mathbb{R}^F : i = a, b, c, d\}$ in (i)-(iv) denotes four point features. Except (i), each points in (ii)-(iv) is associated with an order index, coordinates, and a feature, let $\mathbf{K} = \{k_i \in \mathbb{R}^F : i = \alpha, \beta, \gamma, \delta\}$ is the convolution kernel, $Conv(\cdot, \cdot)$ is a weighted element-wise sum. Traditionally convolving against irregular domains can be denoted as:

$$\begin{aligned}
 f_{ii} &= Conv(\mathbf{K}, [f_a, f_b, f_c, f_d]^T) \\
 f_{iii} &= Conv(\mathbf{K}, [f_a, f_b, f_c, f_d]^T) \\
 f_{iv} &= Conv(\mathbf{K}, [f_c, f_a, f_b, f_d]^T).
 \end{aligned} \tag{4}$$

Note that $f_{ii} \equiv f_{iii}$ holds true for all cases which deserts shape information, while $f_{iii} \neq f_{iv}$ holds true for most cases which reveals variance to point ordering. Hence, feature learning from irregular domains is the core of point cloud-based methods. Specifically, these methods can be further

divided into four categories: multi-view-based, voxel-based, point-based, and point-voxel-based methods on the basis of representation learning from point clouds.

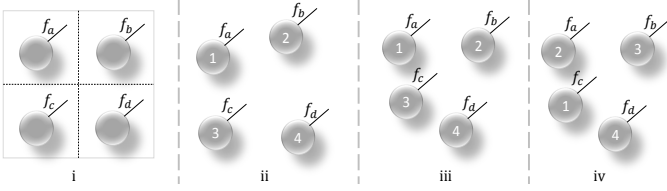


Fig. 8: The effects of convolving against regular grids (i) and point clouds (ii-iv) [20].

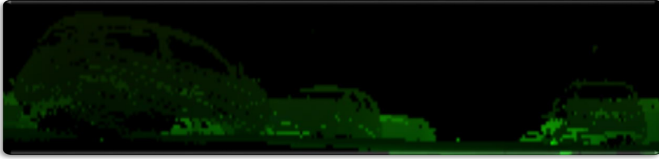


Fig. 9: Visualization of point clouds from front view. Front view with a shape of $3 \times W \times H$ encodes height, distance, and reflectance intensities. Front view can be obtained by the algorithm 3 under LiDAR coordinates. The original image corresponding to the visualized point cloud can be found in 4.

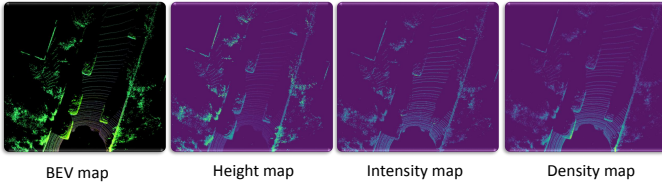


Fig. 10: Visualization of point clouds from bird's eye of view. Height map encodes height information of z -axis, intensity map encodes LiDAR reflection intensity of each LiDAR points, and density map encodes statistics within each grid cell. These maps have a shape of $1 \times W \times H$. BEV map with a shape of $3 \times W \times H$ is the concatenation of three aforementioned maps. All these maps can be obtained by the algorithm 2 under LiDAR coordinates. The original image corresponding to the visualized point cloud can be found in 4.

Multi-view-based Methods. These methods first convert a sparse point cloud into either front view (see algorithm 3) or Bird's Eye View (BEV) (see algorithm 2) representation, which is densely in grids. The idea is intuitive and simple for the sake of leveraging CNNs and standard 2D detection pipeline.

Li et al. proposed VeloFCN [36], which converts a point cloud into front-view 2D feature map, then resorts to the off-the-shelf 2D detectors. To alleviate the problem of occlusions due to overlaps, Yang et al. proposed PIXOR [37], which rasterizes the point cloud into more compact 2D BEV representation. Once discretization, a standard 2D detection pipeline is applied. PIXOR benefits from conversion of point clouds in BEV perspective with an advantage of less scale ambiguity and minimal occlusions. Whereas, according to

algorithm 2, considerable information on vertical axis may be neglected when generating a BEV map. Hence, it is may not a feasible choice for pedestrians, road signs, and objects under overpasses, etc., since these enumerated cases from such a perspective may only be a few points after sampling at a certain height (see algorithm 2), which is obviously not conducive to the network feature extraction.

Voxel-based Methods. These methods generally transform the irregular point clouds to the volumetric representations in compact shape to efficiently extract point features for 3D detection via 3D Convolutional Neural Networks (3D CNNs). It is believed that voxel-based methods are computationally efficient, at the cost of degrading the fine-grained localization accuracy because of the information loss during discretization [23, 40].

Before introducing specific methods, we first must start with several basic concepts, because they run through the whole process of voxel-based Methods. Let p be a point in a point cloud \mathcal{P} with the 3D coordinates (x, y, z) and reflectance intensities r , where $\mathcal{P} = \{p_i = [x_i, y_i, z_i, r_i] \in \mathbb{R}^4 : i = 1, \dots, N\}$. A point cloud \mathcal{P} is first evenly divided into spatial resolution of $L \times W \times H$. Let $v = \{p_i = [x_i, y_i, z_i, r_i]^T \in \mathbb{R}^4 : i = 1, \dots, t\}$ be a non-empty voxel comprising t points ($t \leq \mathcal{T}$) and $[v_L, v_W, v_H] \in \mathbb{R}^3$ be the spatial volume of a voxel, the voxel indices of each point p_i in \mathcal{P} is denoted as $\{\bar{p}_i = (\lfloor \frac{x_i}{v_L} \rfloor, \lfloor \frac{y_i}{v_W} \rfloor, \lfloor \frac{z_i}{v_H} \rfloor) : i = 1, \dots, N\}$, where $\lfloor \cdot \rfloor$ indicates floor function, then iteratively determine which voxel a certain point p_i belongs to according to the associated index. If the points within each voxel reaches the occupancy \mathcal{T} of a voxel, discard p_i directly, otherwise, assign the point p_i to the voxel. Such a many-to-one mapping algorithm (hereafter called hard voxelization) is widely adopted by SECOND [41], Pointpillars [43] and all their successors, which by nature presents three intrinsic limitations [42]: 1) Given points and voxels are thrown away when they exceed the allocated capacity, useful information for detection could possibly be forsaken. 2) Non-deterministic voxel embeddings with points and voxels being stochastically dropped, could lead to jitteriness of detection models. 3) Unavailing zero-padding squanders unnecessary computation somewhat. For simplicity, SA-SSD [40] directly quantizes each point p_i to tensor index by regarding each p_i as a nonzero entry. The shared index of multiple points will be overwritten in place by the latest point. Recently, Zhou et al. [42] proposed a novel dynamic voxelization to overcome preceding limitations, The differences between hard voxelization and dynamic voxelization are illustrated in Fig. 11.

Voxel-wise representation is nothing but aggregate point-wise features into voxel-wise features. As far as we know, there exists three operators at present. As shown in Fig. 12, 1) **Mean operator.** All inside point features with the 3D coordinates and reflectance intensities of a certain voxel are directly calculated for the mean, (i.e., the centroid), denoted as (c_x, c_y, c_z) . (e.g., SECOND[41]) 2) **Random sampling.** A point within the voxel is randomly selected on behalf of the voxel feature. (e.g., SA-SSD [40]) 3) **MLP operator.** The point-wise features \hat{p}_i within v are then transformed by a

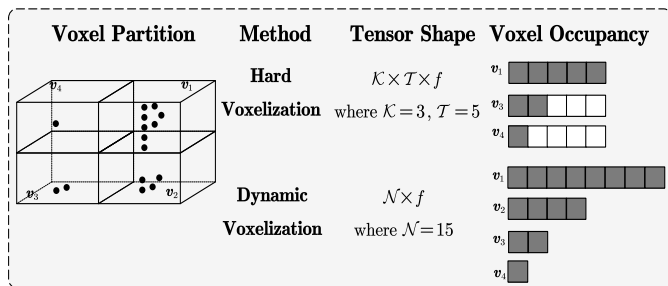


Fig. 11: Comparisons of hard voxelization and dynamic voxelization [42]. Specifically, assume that 3D space is evenly divided into four voxels, which is indexed as v_1, v_2, v_3, v_4 . Hard voxelization may randomly drops 3 points in v_1 and discards v_2 with $15f$ memory usage if we set the occupancy of a voxel \mathcal{T} to 5 and the maximum kept voxels \mathcal{K} to 3 for a whole point cloud for memory cost saving. Whereas, dynamic voxelization gets rid of unstable voxel embeddings via keeping all points during voxelization with memory usage $15f$.

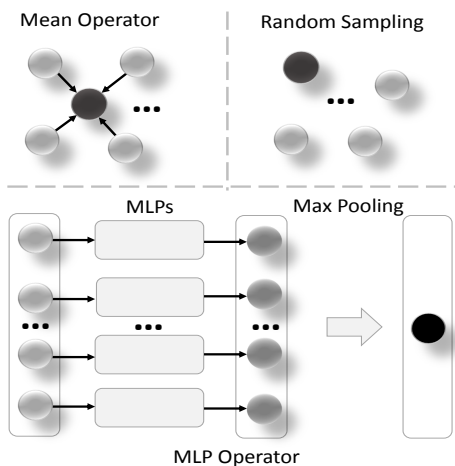


Fig. 12: Illustration of voxel-wise representations via three aggregation operators.

PointNet [5] block to generate voxel-wise high level semantic features as:

$$f = \max \{ \text{MLP}(G(\hat{p}_i)) \in \mathbb{R}^m : i = 1, \dots, \mathcal{T} \} \quad (5)$$

Optionally, the initial voxel representation can be augmented by the relative offset of the centroid (c_x, c_y, c_z) as: $v = \{ \hat{p}_i = [x_i, y_i, z_i, r_i, x_i - c_x, y_i - c_y, z_i - c_z]^T \in \mathbb{R}^7 : i = 1, \dots, t \}$, where $G(\cdot)$ denotes randomly sampling at most \mathcal{T} points in order to keep the number of points within each voxel be the same. $\text{MLP}(\cdot)$ denotes a stacked multi-layer perceptron network composed of a linear layer, a Batch Normalization (BN) layer, and a Rectified Linear Unit (ReLU) layer. The along-channel max-pooling operation $\max(\cdot)$ aggregates all inside point-wise features into voxel-wise features f (e.g., Voxelnet [45], Pointpillar [43], and F-ConvNet [46], etc.).

Zhou et al. took the first lead to propose an end-to-end trainable network named VoxelNet [45], as shown in Fig. 15(a). Instead of manual feature engineering as most previous works do, VoxelNet learns a informative feature representation by

three components: (1) Feature learning network, (2) Convolutional middle layers, and (3) Region proposal network. Feature learning network divides a point cloud into equally spaced 3D voxels, and newly introduce a PointNet-like Voxel Feature Encoding (VFE) layer to transform a set of points into a vector that encodes the shape of the surface within each voxel. The convolutional middle layers introduces more contextual shape description by aggregating voxel-wise features within an expanding receptive field. Finally, the Region Proposal Network (RPN) takes as input the 3D CNN feature volumes and outputs the encouraging 3D detection results. Although the VoxelNet is the seminal work in 3D object detection, its drawbacks are: the cubically computational complexity of 3D convolutional network imposes increased memory usage and efficiency burdens on the computing platform. Later on, Yan et al. proposed SECOND [41] to reduce memory consumption and accelerate computational speed via sparse convolutional operation. As illustrated in Fig. 15(b), They first gathered the original sparse data directly in an ordered fashion with its corresponding coordinates being recorded, then they performed a General Matrix Multiplication (GEMM) algorithm to convolve against the gathered data before scattering the data back. Sparse convolutional operation opts to take advantage of the sparsity of a point cloud to only convolve against non-empty voxels rather than perform on all voxels as traditional 3D convolutions do. Although SECOND leverages sparse convolution operation to get rid of unnecessary computation squandered by unavailing zero-padding voxels compared with VoxelNet [45], the expensive 3D convolutions remain, hindering the further improvement of speed. Subsequently, Pointpillars was proposed to remove this bottleneck. H. Lang et al. proposed PointPillars [43], which encoded point clouds into vertical columns, namely, pillars, a special partition of voxels in essence, in order to take advantages of standard 2D convolutional detection pipeline. PointPillars consists of three main components as VoxelNet does: (1) A feature encoder network, (2) a 2D convolutional backbone, and (3) A detection header. The feature encoder network organizes a point cloud in vertical columns, then scattering the pillars back to its original localization to create a pseudo-image in a BEV perspective. The 2D convolutional backbone comprises two sub-networks: one downsamples the pseudo-image while the other upsamples and concatenates the downsampled features. The detection header regresses 3D boxes the same as its 2D counterpart. Albeit Pointpillars achieves a 2-4 fold runtime improvement at 62 FPS¹ via getting rid of traditional 3D convolutions used in VoxelNet [45], it suffers poor information perception problem in pillar partition. As a result, the subsequent literature is prone to encode a point cloud into voxels instead of pillars in the light of tradeoff between efficiency and accuracy [44].

Shi et al. proposed Part- A^2 [24]. Motivated by the observation that intra-object part locations can be provided by the 3D bounding box annotations accurately without any occlusions, two stages are delicate designed: the part-aware stage and the part-aggregation stage. Specifically, Part- A^2 utilizes a UNet-like [72] architecture to convolve and deconvolve non-empty

¹FPS denotes Frames Per Second.

voxels for foreground points segmentation and part prediction. Simultaneously, coarse 3D proposals are generated via an extra RPN header. In the part-aggregation stage, a subtle RoI-grid pooling module is presented to eliminate the ambiguity of 3D bounding boxes and learn the spatial correlations of the points within 3D proposals. Last, 3D sparse convolution [41] is applied to aggregate the part information for scoring and refining locations. Ye et al. proposed HVNet [47], which consists of three components: 1) Multi-scale voxelization and feature extraction 2) Multi-scale feature fusion and dynamic feature projection 3) A detection header. Specifically, HVNet voxelizes a point cloud at different scales first, then for each scale, a voxel-wise feature is computed by aggregating the information of each point within a voxel, resorting to an Attentive Voxel Feature Encoder (AVFE). Then these high level semantic features are scattered back to their original localization, forming a pseudo-image according to the corresponding index records. Last, HVNet employs FPN [70] as the backbone to predict final instances. These strategies enable HVNet to outperform all existing LiDAR-based one-stage methods in terms of *Cyclist* on KITTI benchmark with a real time inference speed of 31FPS. Although HVNet ranks 1st on the KITTI test server associated with the *Cyclist* category, there still exists a far cry from the state-of-the-art LiDAR-based methods on the *Car* leaderboard. Given that the car category predominates the whole KITTI dataset [19, 51], it will be more persuasive to compare on the *Car* category.

Point-based Methods. These methods generally consume raw point clouds leveraging two types of backbone: PointNet(++) and its variants or Graph Neural Networks (GNNs). Usually, they retain the geometry of the original point cloud as much as possible. Nevertheless, point retrieval in 3D space is hostile to efficient hardware implementations compared with volumetric grids [73].

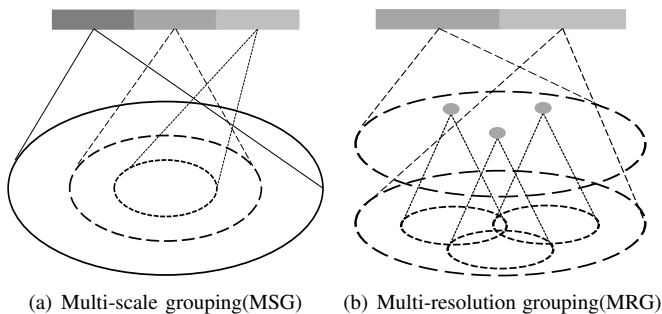


Fig. 13: PointNet(++)[74] applies PointNet [5] recursively in a hierarchical manner. In particular, the density adaptive layers, i.e., the Multi-Scale Grouping(MSG) and Multi-Resolution Grouping(MRG), enable PointNet and its variants to adaptively capture local structures and fine-grained patterns of point clouds.

In 2017, Qi et al. proposed PointNet [5], which is a pioneer in terms of learning over point sets. PointNet enables the network to directly consume raw point clouds and learn 3D representations from a point cloud for classification and segmentation without converting a point cloud into volumetric

grids or other formats. As shown in 13, the improved version, PointNet(++) [74], applies PointNet recursively in a hierarchical manner. In particular, the density adaptive layers, i.e., the Multi-Scale Grouping (MSG) and Multi-Resolution Grouping (MRG), enable PointNet and its variants to adaptively capture local structures and fine-grained patterns of point clouds. Later on, a series of point-based methods sprang up for 3D object detection on the basis of PointNet due to its generalizability to complex scenes. Hence, point-based methods (e.g., PointRCNN [22], 3DSSD [39]) are powered by PointNet(++) [5, 74] and its variants to directly extract discriminative features from raw point clouds. In this paradigm, usually Set Abstraction (SA) layers are utilized for downsampling points and Feature Propagation (FP) layers are applied for broadcasting features to the whole scene via upsampling. Afterwards, they leverage a 3D region proposal network to generate high-quality proposals centered at each point for the further refinement in the final stage. These methods could obtain flexible receptive field by the stacked SA modules at the price of higher computation cost compared with voxel-based methods.

Algorithm 1 Farthest Points Sampling

Require: $\mathcal{P} = \{p_1, p_2, \dots, p_{\mathcal{N}}\}$ is a set of point cloud data, where \mathcal{N} is the number of points. Each point is presented by a C -length vector. $k \in \mathbb{N}$ is the number of samples. $D = (D_1, D_2, \dots, D_{\mathcal{N}})$ is a distance vector containing the distance of each point from a sampled point set. Set $D_n = +\infty, n = 1, 2, \dots, \mathcal{N}$.

Ensure:

- 1: Randomly sample the first point $p_{i_1} \in \mathcal{P}, i_1 \in \{1, 2, \dots, \mathcal{N}\}$.
- 2: **for** $s = 1, 2, \dots, k - 1$ **do**
- 3: **for** $n = 1, 2, \dots, \mathcal{N}$ **do**
- 4: $d(n, i_{s+1}) = \sum_{j=1}^C (p_n(j) - p_{i_{s+1}}(j))^2$.
- 5: **if** $d(n, i_{s+1}) < d(n, i_s)$ **then**
- 6: $D_n = d(n, i_{s+1})$.
- 7: **end if**
- 8: **end for**
- 9: Sample the next farthest point's index:

$$i_{s+1} = \arg \max_{n \in \{1, 2, \dots, \mathcal{N}\}} D_n.$$

10: **end for**

11: **return** Sampled farthest points $(p_{i_1}, p_{i_2}, \dots, p_{i_k})$.

Shi et al. proposed PointRCNN [22], as shown in Fig. 15(c). PointRCNN is a typical point-based two-stage detection framework, elegantly transplants the idea of classical 2D detector, Faster RCNN [13], into 3D detection task, taking point clouds only as input: (1) Since 3D object instances in point clouds are well separated by annotated 3D bounding boxes, PointRCNN directly performs semantic segmentation on the whole scene via PointNet(++) architecture to achieve foreground points, generating a set of high-quality 3D proposals in a bottom-up fashion. (2) PointRCNN leverages 3D region of interest pooling operation to pool points and corresponding semantic features of each proposal for further box refinement and confidence prediction. The limitation of PointRCNN is

the inference time: both the backbone, PointNet(++), and refinement modules in stage two are time consuming. Yang et al. proposed 3DSSD [39]. The main contributions of 3DSSD are: (1) It safely removes FP layers, which is regard as the main bottleneck of speed for point-based methods, via fusing Euclidean metrics (refer to as D-FPS* in 3DSSD [39]) and features metrics (refer to as F-FPS* in 3DSSD [39]) together when performing Furthest Point Sampling (FPS*)² specified in algorithm 1 to make up the loss of interior points of different foreground instances during downsampling. (2) An anchor-free regression header is developed to reduce memory consumption and boost the accuracy further. 3DSSD is more than 25 FPS, 2× faster than PointRCNN, around 13 FPS, which makes it possible to be widely used in real-time systems.

A large body of literature [75–79] has looked into leveraging GNNs for classification and semantic segmentation from point clouds. Since GNNs has a strong reasoning ability over Non-Euclidean data (e.g., Point Clouds) [80]. Point cloud-based 3D object detection is another area in which graph-based methods are poised to make a large impact over the next few years. Currently, using GNNs for 3D object detection is still largely unexplored [81, 82], nevertheless. Shi et al. proposed Point-GNN [25], which utilizes GNNs to preserve the irregularity of a point cloud without quantization. Point-GNN leverages a graph neural network to encode a point cloud by regarding each point within the point cloud as graph vertex. Points that lie within a given cut-off distance are connected to form the graph edges. Point-GNN comprises three steps: (1) Constructing graph from a downsampled point cloud, (2) Updating each vertex so that the message can flow between neighbors for detecting the category and localization, and (3) Merging 3D bounding boxes from multiple vertices. Although Point-GNN pioneered a new stream line for 3D object detection, its challenges are tricky: the time of constructing graph and inference within iterations are usually intolerable and it takes almost one week to completely train the model claimed in the paper. Note that point-based methods are sensitive to translation variance. To alleviate the dilemma, Point-GNN proposed an auto-registration mechanism to predict alignment offsets appended to neighbors’ relative coordinates via structural features of the center vertex. 3DSSD predicts shifts for foreground points supervised by the relative locations between those interior points and their corresponding center within a instance.

Point-voxel-based Methods. Point-voxel-based methods represent a new growing trend for learning representations from a point cloud. In 2019, Liu et al. proposed PVConv [73], PVConv fuses the merits of voxels and points together. On the one hand, voxel-based methods are vulnerable to the parameters of voxels, e.g., low resolution results in coarse-grained localization accuracy, whereas, high resolution increases cubical computation cost. On the other hand, point-based methods can easily preserve the irregularity and locality of a point cloud opting to either set abstraction or PointNet-like block, providing fine-grained neighborhood information. In fact, such integration has been proved to be effective by

²We name Furthest Point Sampling FPS* to avoid ambiguity.

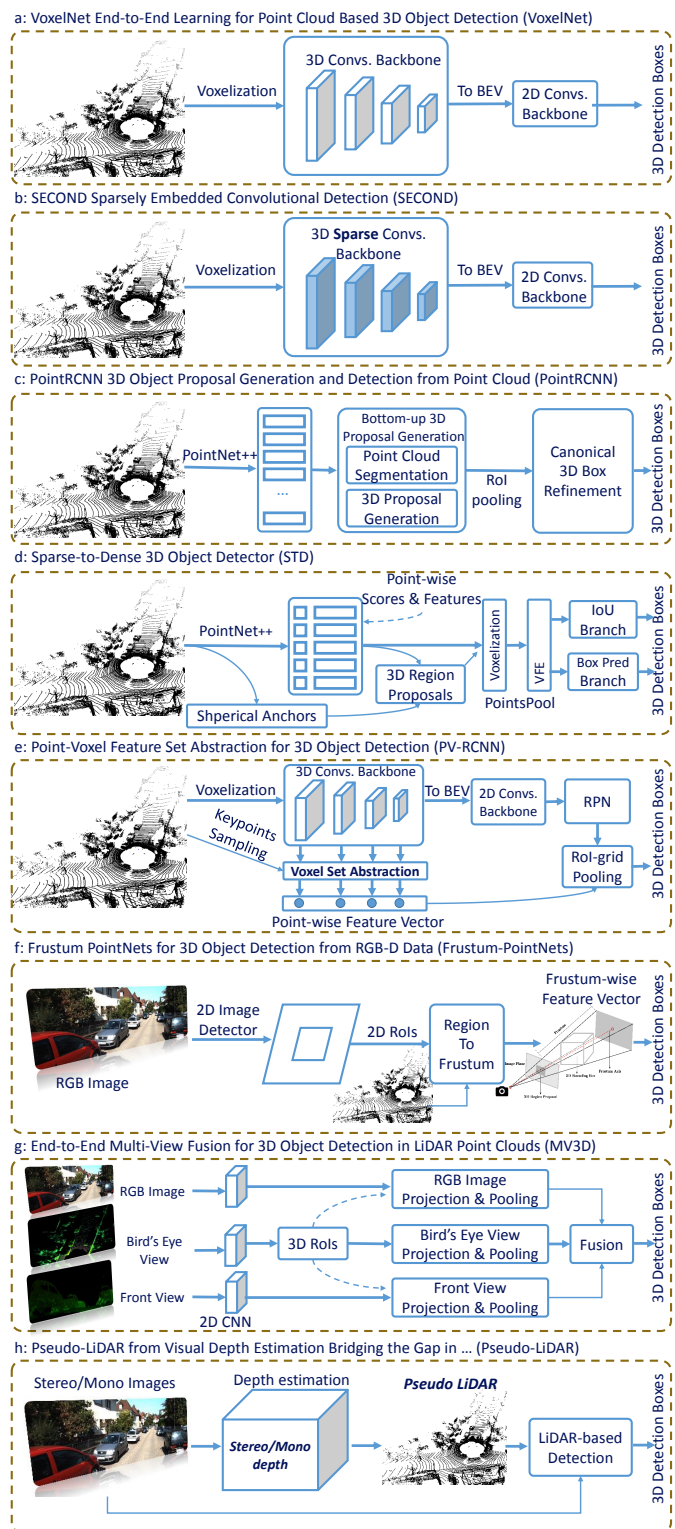


Fig. 15: Representatives of 3D object detectors. From top to bottom: a) VoxelNet [45], b) SECOND [41], c) PointRCNN [22], d) STD [38], e) PV-RCNN [23], f) Frustum-PointNets [56], g) MV3D [52], h) Pseudo-LiDAR [64].

multiple literature [23, 38, 40, 63] in practice.

Chen et al. proposed Fast Point R-CNN [63], which benefits from volumetric representation and raw dense coordinates respectively. The first stage, termed VoxelRPN, generates a

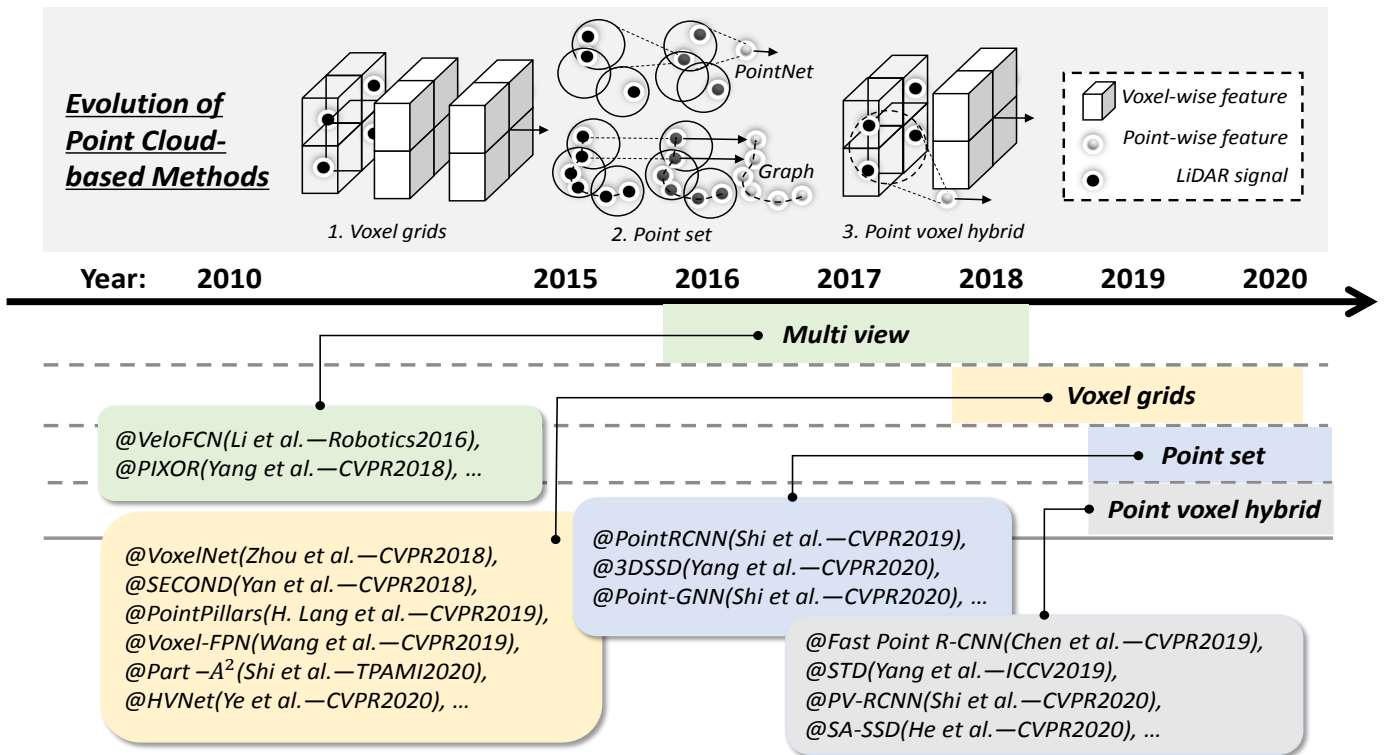


Fig. 14: Evolution of point cloud-based methods: 1) Voxel grids, 2) Point set, 3) Point voxel hybrid. Detectors in this figure: VeloFCN [36], PIXOR [37], VoxelNet [45], SECOND [41], PointPillars [43], Voxel-FPN [44], Part-A² [24], HVNet [47], PointRCNN [22], 3DSSD [39], Point-GNN [25], Fast Point R-CNN [63], STD [38], PV-RCNN [23], SA-SSD [40].

small set of high-quality proposals via voxelizing the whole scene into regular grids in a bottom-up fashion. Given the initial predictions, a light-weight PointNet, RefinerNet, is closely designed to effectively fuse the interior points and their corresponding convolution feature via attention mechanism, with the loss of localization information in the first stage being supplemented. Fast Point R-CNN runs at 15 FPS. Yang et al. proposed STD [38], as shown in Fig. 15(d). The pipeline of STD is very similar to PointRCNN. The main innovations of STD is spherical anchor, which is more generic to achieve a high recall than rectangular one, regardless of heading angle. STD possesses excellent performance, especially on the hard set. Shi et al. proposed PV-RCNN [23], as shown in Fig. 15(e), which deeply integrates the effectiveness of 3D Sparse Convolution [41] and the flexible receptive fields of PointNet-based set abstraction to learn more discriminative point cloud features. Specifically, PV-RCNN utilizes a 3D sparse convolution as the backbone to encode the whole scene, the same as SECOND [41]. Then two innovative operations, the voxel-to-keypoint scene encoding and key-point-to-grid RoI feature abstraction are applied for computation cost saving and localization refinement. In particular, the Voxel Set Abstraction (VSA) module is adopted to aggregate the multi-scale semantic voxel-wise features from 3D CNNs into keypoint features. Note that the keypoints are selected via FPS* algorithm 1 from the original point cloud. PV-RCNN ranks 1st on the *Car* 3D detection leaderboard and outperforms the second by a large margin as of Jul. 10th, 2020. The absolute improvements

demonstrate the effectiveness of integrating the best of two worlds, that is, point-based methods and voxel-based methods together. He et al. proposed SA-SSD [40]. SA-SSD explicitly leverages the geometric information of a 3D point cloud via an auxiliary network. Specifically, SA-SSD first progressively downscales point clouds in a sparse convolutional fashion. Then the downscaled convolutional features are discretized evenly to point-level representations with primitive voxel-wise unit. Next, the points within a 3D ground truth bounding box, along with the offsets from the box center provide point-level supervisions for jointly optimizing the auxiliary network: the former forces the features to be sensitive to the object boundary while the latter establish the intra-object relationships between voxels. It is ingenious for the auxiliary network to detach after training, running at 25 FPS and with no extra computation overhead being introduced in the inference stage. All along, the mismatching problem between the classification score and corresponding localization accuracy is salient, regardless of 3D object detection [23, 38, 40] or its 2D counterpart [83]. As GS3D [31] notes, given that the classification and box regression branch are trained in parallel, Non Maximum Suppression (NMS) is likely to remove high-quality bounding boxes with low classification score. To alleviate the discordance, STD [38] adds a 3D Intersection-over-Union (IoU) prediction branch to multiply each box's confidence with its predicted 3D IoU. PV-RCNN [23] directly uses 3D IoU as the training targets. SA-SSD [40] develops a part-sensitive warping operation to sample features along

channels for the mean in order to perform further classification to relief such discrepancy.

In summary 14, voxel-based methods are easily amenable to efficient hardware implementations with distinguished accuracy and latency, but inevitably suffering quantization loss considering that a number of points beyond the voxel occupancy will be discarded. At the same time, the process of voxelization is more sensitive to the selection of parameters, i.e., the length, width and height of a voxel; Point-based methods more reasonably retain the original geometry information of a point cloud. For methods powered by pointnet(++), the critical modules, FPS* and feature propagation layers are more time-consuming than voxelization in terms of consuming a point cloud; as for those powered by GNNs, intuitively, not only the correlations between points, but also the more intricate spatially-local structure, that is, the “vertex-edge” information is captured simultaneously. The 3D shape will be more easily perceived, at the cost of taking longer feedforward time than those taking pointnet(++). as the backbone.

C. Multimodal Fusion-based Methods

Nowadays, 3D object detection for autonomous driving largely relies on LiDARs in the light of providing informative surrounding information. Albeit precise, it is not sensible enough to be over-reliant on a single sensor due to an inherent safety risk(e.g., sabotage, adverse conditions, and blind spots, etc.). In addition, the low resolution of a point cloud at the long ranges and poor texture information also pose a great challenge. Naturally, the most promising candidate is on-board stereo or monocular cameras, which provide fine-grained texture as well as RGB attributes simultaneously. Cameras suffer depth ambiguity by nature, though. Besides, stereo or monocular cameras are several orders of magnitude cheaper than LiDARs, with a high frame rate and a dense depth map. One persuasive case is illustrated in Fig. 16, it is more difficult to distinguish the pedestrian and signpost in the LiDAR modality when it comes to a long distance. Obviously, each sensor type has its defects, the joint treatment is seen as a possible remedy to failure modes. Literature [84] even states that multimodal fusion provides redundancy during difficult conditions rather than just complementary. Although exploiting the synergies is a compelling research hotspot, still, it is non-trivial to consolidate the best of two worlds at present in the light of misalignment view, namely, camera view and LiDAR bird’s eye of view.

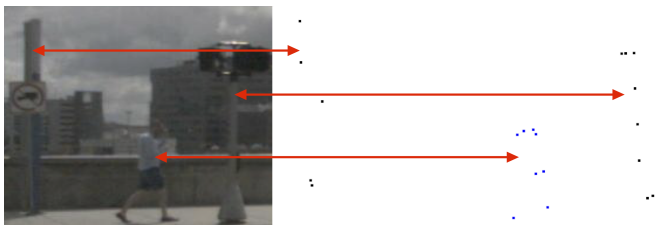


Fig. 16: A scene from the nuScenes [84] where the pedestrian and signpost are clearly identifiable in image modality. Image from Vora et al. CVPR2020 [57].

Deep neural networks exploit the property of compositional hierarchies from natural signals [85], in which fusion strategies may vary. Generally, two classes of fusion schemes exist, namely, early fusion and late fusion [6, 7, 26, 52, 86]. The former combines multimodal features before fed into a supervised learner, whereas the latter integrates semantic features obtained by separately trained supervised learners [86], as illustrated in Fig. 17.

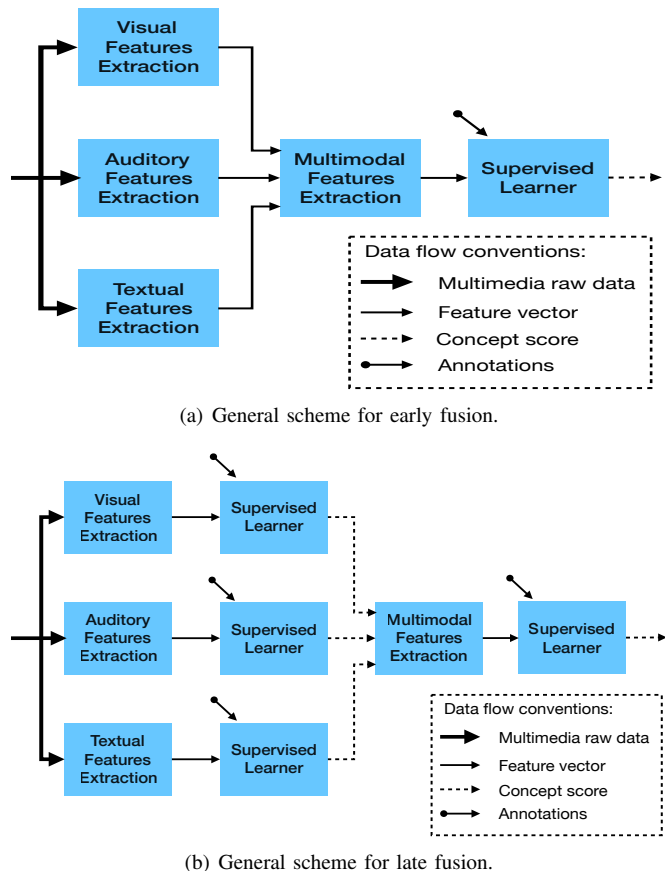


Fig. 17: Two traditional fusion schemes for modalities

Note that diverse fusion variants consistently emerges in 3D object detection, the schemes aforementioned may not apply. For instance, pointpainting [57] is a sequential fusion method, which neither applies to early fusion nor late one. Hence, we define two new categories: sequential fusion and parallel fusion. In the sequel, we first give a definition for each scheme, and then judiciously analyze corresponding methods under our newly defined paradigms.

Sequential Fusion-based Methods. These methods exploit multi-stage features in a sequential manner, in which the current feature extraction depends heavily on the previous stage.

Qi et al. proposed Frustum PointNets [56], as shown in Fig. 15(f). Frustum PointNets first leverages a standard 2D CNN object detector to extract 2D regions, then transforms 2D regional coordinates to the 3D space to crop frustum proposals. Next, each point within the frustum is segmented by a PointNet-like block to obtain interest points for further regression. Frustum PointNets resorts to mature 2D detection

methods to provide prior knowledge which to a certain extent, reduces the 3D search space and inspires its successors (e.g., F-ConvNet [46]). Although Frustum PointNets is very innovative, the drawbacks of such a cascade approach are: Frustum PointNets heavily relies on the accuracy of 2D detectors. Vora et al. proposed PointPainting [57], which leverages semantic segmentation information from images to consolidate point clouds. Specifically, PointPainting first turns to semantics network for per pixel classification, and then the relevant segmentation score, which in fact serves as compact summarized features of the image is appended to the LiDAR points via projecting the LiDAR points into the segmentation mask directly, “painting”, vividly. Last, an arbitrary LiDAR-based 3D detector is deployed for instance localization and classification. Although PointPainting consistently enhances the existing networks (e.g., PoinRCNN [22], SECOND [41], Pointpillar [43]) by utilizing segmentation scores instead of RGB attributes. PointPainting is not an end-to-end training. Besides, low semantic segmentation accuracy will deteriorate the model itself.

Another attempt is Pseudo-LiDAR. Wang et al. proposed Pseudo-LiDAR [64], as illustrated in Fig. 15(h), which first uses the pyramid stereo matching network (PSMNET) [87] to obtain depth estimation. Then it back-projects all the pixels in the image into 3D coordinates in space via the disparity map, which is referred to as pseudo-LiDAR signals. At last, existing LiDAR-based detector is applied. It is reported that Pseudo-LiDAR increases image-based performance within 30m range by 52% (from 22% to an unprecedented 74%) on the popular KITTI benchmark. The idea of Pseudo-LiDAR is simple but compelling. It argues that it is the data representation not the discrepancy in depth estimation that matters, which mainly results in the performance gap between stereo images and LiDARs. Pseudo-LiDAR helps us reexamine the off-the-shelf monocular/stereo-based detectors and sensors, which provides some important enlightenments to the current 3D perception systems. Although pseudo-LiDAR signals are a promising alternative, a notable performance gap still exists compared with the real LiDAR signals, according to the experiments. Later, You et al. proposed Pseudo-LiDAR++ [65]. The Pseudo-LiDAR++ was proposed to align the faraway objects, given that the depth estimation error grows quadratically at long ranges. The main contribution of Pseudo-LiDAR++ is that it presented a Graph-based Depth Correction (GDC) algorithm, which leverages sparse but accurate LiDAR points (e.g., the 4 laser beams) to de-bias stereo-based depth estimation. Specifically, they project a small portion of sparse LiDAR points, namely “landmarks”, onto pixel locations, and assign them to corresponding 3D Pseudo-LiDAR points as “ground truth” LiDAR depth. Note that the depth of 3D Pseudo-LiDAR points is obtained by stereo depth estimation (PSMNET) [87]. To correct depth values, Pseudo-LiDAR++ first constructs a local graph via k Nearest Neighbors (k NN), then update graph weight under the supervision of “landmarks”. Last, the information propagates over the entire graph at negligible cost. Although Pseudo-LiDAR++ subtly explored a hybrid approach to correct depth bias, it is not an end-to-end approach. Such an issue is then well addressed by Pseudo-LiDAR E2E [88]

in 2020.

Parallel Fusion-based methods. These methods fuse modalities in feature space to obtain one multimodal representation before fed into a supervised learner.

Chen et al. proposed MV3D [52], as shown in Fig. 15(h). MV3D takes a multi-view representation, that is, the bird’s eye view and the front view as well as images as inputs. MV3D first generates a handful set of accurate 3D candidate boxes by utilizing a bird’s eye view representation of a point cloud. Given the high-quality 3D proposals, MV3D crops the corresponding regions from multiple views according to the coordinates of 3D Proposals. Then, a deep multi-view fusion network is employed to fuse the RoI-wise features. Although MV3D exploits multiple view representations of a point cloud, its drawbacks are: MV3D resorts to hand-craft features, which hinders its further improvement and is surpassed by its successors soon. Besides, MV3D does not work well for small objects since they only occupy a fraction of a pixel in the course of progressively downscaling. Later on, Ku et al. proposed AVOD [53]. AVOD is slightly different from MV3D [52] in that it further extends fusion strategy to the early region proposal stage. Specifically, given a set of predefined 3D boxes which are referred to as anchor boxes, two corresponding regions are cropped and resized from both image and BEV feature maps at the top of feature pyramids respectively, and then fused by an element-wise mean operation, then AVOD feeds the fused features into fully connected layers to detect objects. AVOD argues that such a delicate operation allows to generate high recall proposals and benefit localization accuracy, especially for small objects. Although AVOD advanced the fusion strategy resulting in a further improvement of proposal quality, such a regional fusion only happens at the top of the feature pyramids. Whereas, intermediate features can be important for detection [89]. Note that both MV3D and AVOD are RoI-wise level fusion strategies, then pixel-wise fusion is subsequently proposed for synergies in deep. ContFuse is proposed to further fuses multi-scale convolutional features via continuous convolution in a pixel-wise fashion.

Ming et al. proposed ContFuse [58]. which leverages continuous convolution layers, to perform multi-sensor fusion at multiple scales. Such a fusing operation is non-trivial, however, e.g., quite a few discrete pixels in LiDAR BEV feature map are unobservable in camera view as one captures the world’s native 3D structure while the other represents the world onto 2D camera plane. Hence, ContFuse first finds k nearest LiDAR points for each pixel in LiDAR BEV feature map, then retrieves the k corresponding image features by bilinear interpolation according to the coordinates of the source LiDAR points projected onto the images. Next, ContFuse leverages MLP operation to encode interpolated image features, together with continuous 3D geometry offsets between k nearest LiDAR points and the target pixel in LiDAR BEV feature map, to generate the final representation for the target LiDAR BEV pixel. Note that the relative offset is aimed for modeling each point’s contribution to the final representation. Although ContFuse pioneered the modality fusion in terms of leveraging image feature maps and BEV feature maps, such fusion is

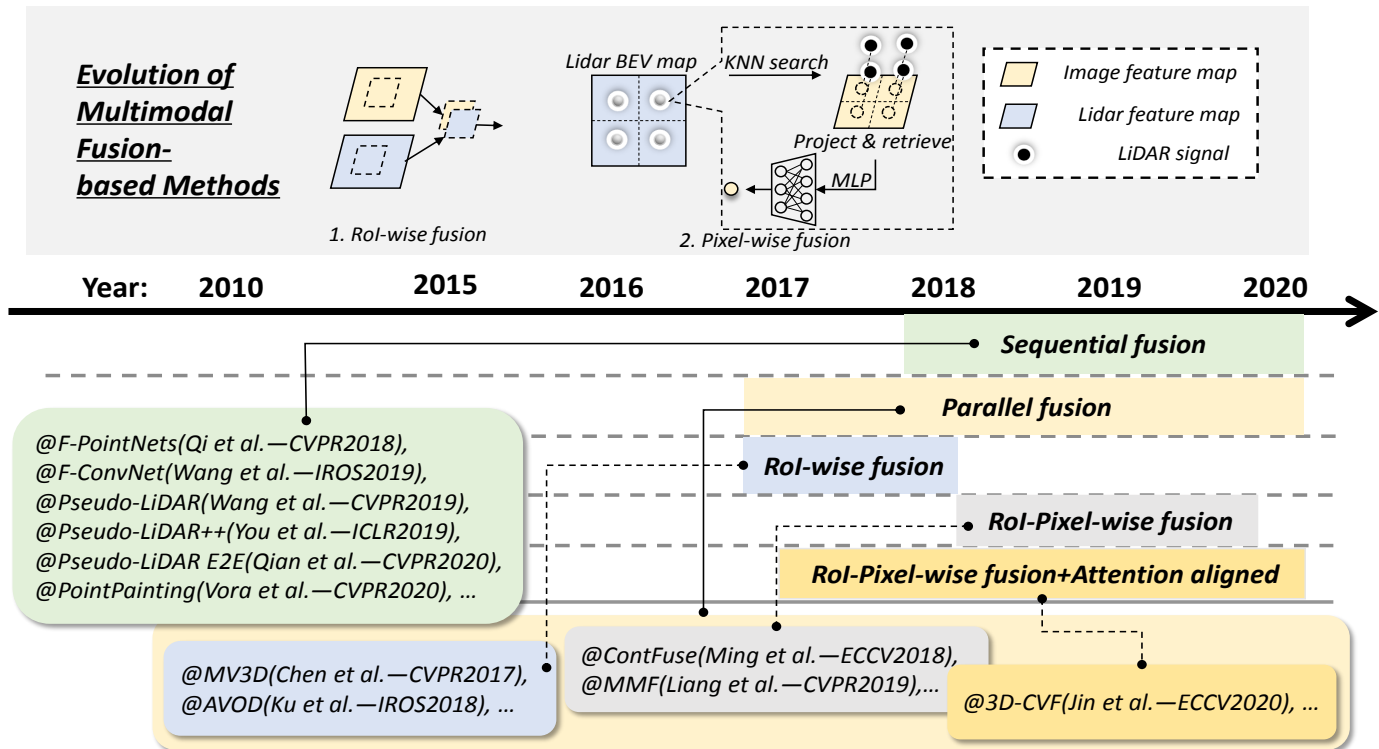


Fig. 18: Evolution of multimodal fusion-based methods: 1) RoI-wise fusion, 2) Pixel-wise fusion. Detectors in this figure: Frustum PointNet [56], F-ConvNet [46], PointPainting [57], Pseudo-LiDAR [64], Pseudo-LiDAR++ [65], Pseudo-LiDAR E2E [88], MV3D [52], AVOD [53], ContFuse [58], MMF [66], 3D-CVF [67].

likely to suffer the problem of sparsity at long range in that LiDAR signals are by nature constrained to the 64 or 128 sparse rotating laser beams.

Liang et al. proposed MMF [66], which is a multi-task and multi-sensor fusion architecture. MMF exploits multiple related tasks (e.g., ground estimation, depth completion, and 2D/3D object detection). It turns out that these tasks are complementary for better representation learning via information fusion of various levels. Specifically, MMF implements the fusion at two levels: point-wise feature fusion and RoI-wise feature fusion. The former utilizes LiDAR points as the intermediate bridge: for each pixel in the BEV feature map, MMF retrieves the corresponding image feature via projecting the nearest LiDAR points onto the image. The latter performs ROIAlign operation on the image and BEV feature maps respectively to extract regions of interest for fusion and further refinement. In addition, the auxiliary tasks, ground estimation and depth completion, facilitate feature fusion via providing geometric priors and cross-modality correlations. MMF runs at 10 FPS. Although MMF integrates multi-task to benefit 3D detection task, its drawbacks are: Depth completion indeed densifies the LiDAR points, especially at long ranges, but to what extent the estimation error will affect the robustness of the system is agnostic. Jin et al. proposed 3D-CVF [67]. Specifically, 3D-CVF first downscales point clouds $8\times$ in a 3D sparse convolution fashion after voxelization to encode 3D feature volumes into 2D birds view feature maps, and resorts to pre-trained ResNet-18 [69] to extract the corresponding

image features in parallel. One of the most challenges to fuse these two modalities is misalignment view. To this end, the first stage of 3D-CVF presents auto-calibrated feature projection, which is a simplified version of continuous fusion layer [58] in essence, to align camera view and LiDAR BEV view. Particularly, in ContFuse [58], k nearest LiDAR points are extracted for each pixel as a bridge in LiDAR BEV feature map, then these k LiDAR points are projected to camera view to retrieve pixel-wise image features. And to obtain the final corresponding feature, a PointNet-like block is applied to the k pixel-wise image features. Nevertheless, as for 3D-CVF, the center coordinate of voxel grid is directly projected onto image plane to interpolate the camera features. Simultaneously, 3D-CVF employs an adaptive attention mechanism to filter information from image features and convolved 3D point clouds features. Given the proposals in the first stage, 3D RoI grid pooling is utilized to transfer and fuse image features to the aligned LiDAR BEV feature map for RoI-wise fusion, with more spatial information being supplemented. Although 3D-CVF shows significant performance gains over existing fusion-based works, gap still exists compared to LiDAR based methods (e.g., PV-RCNN). Note that “feature blurring” [57] is a common problem existing in all pixel-wise fusion methods, that is, two LiDAR points in 3D space that are far away from each other may roughly correspond to the same pixel in the image location, which contributes to bias inevitably.

In summary 18, there is no consensus on which paradigm is better. Sequential fusion-based methods integrate features

in a sequential fashion, in which current phase is dependent on previous one. In such a paradigm, model architecture usually can not be trained end-to-end in the light of high memory requirements. Besides, a tighter coupling between different stages is one of typical characteristics existing in all sequential fusion-based methods, that is, poor performance in the previous stage could deteriorate the remaining stages. In addition, informative intermediate features are largely forsaken, which is plausibly crucial for object detection. Parallel fusion-based methods integrate features in one multimodal representation. Only one learning phase is required. Whereas, view misalignment among sensors is usually tricky.

V. BENCHMARK EVALUATION

This section covers commonly used metrics, and extensive apples-to-apples comparison of the state-of-the-arts. Finally, the future research directions are going to be judiciously identified based on aforementioned analysis of the surveyed works, together with emerging datasets.

KITTI [19, 51]: Since all methods specified in Section IV perform their experiments on the basis of KITTI, we bring KITTI out alone from emerging datasets. KITTI dates back to 2012, covering most of the 3D tasks (e.g., lane detection, depth estimation and completion, object tracking, and domain adaptation, etc.). In addition, each track has expedited abundant open resources. Its protocol has inspired almost all subsequent datasets (e.g., nuScenes [84], Lyft dataset [90], Waymo open dataset [91], and Applloscape dataset [92]) somewhat. Hence, the pioneering KITTI Dataset has become the industry de facto intended for the autonomous driving: equipped with four high resolution video cameras, a Velodyne laser scanner and a GPS/IMU localization unit[19], KITTI acquires 7,481 training images and 7,518 held-out testing images in addition to the corresponding raw point clouds with three categories of *Car*, *Pedestrian* and *Cyclist*. These three categories are further divided into three levels of difficulty, *easy*, *moderate* and *hard*, according to the level of occlusion and truncation.

A. Metrics

The ideology of object detection derived from the same origin, regardless of 2D/3D object detection, so do the metrics. In fact, the well established Average Precision (AP) described in [93] is the most common metric used to evaluate the performance of an object detector. Before introducing AP, some basic concepts should be reviewed in the the scope of object detection.

Rotated Intersection over Union (IoU_{3D}) As shown in Fig. 19, the rotated IoU_{3D} evaluates the rotated overlap between a ground-truth bounding box \mathcal{B}_{gt} (in green) and a detected bounding box \mathcal{B}_p (in red), that is:

$$J(\mathcal{B}_p, \mathcal{B}_{gt}) = \text{IoU}_{3D} = \frac{\text{rotated 3D area}(\mathcal{B}_p \cap \mathcal{B}_{gt})}{\text{rotated 3D area}(\mathcal{B}_p \cup \mathcal{B}_{gt})}. \quad (6)$$

Using the IoU stated above, we can define what True Positive (TP) and False Positive (FP) are: a detection is considered as TP with $\text{IoU} \geq \text{threshold}$, otherwise is FP. (e.g., for KITTI, the threshold is set to 0.7 for car, 0.5 for pedestrians

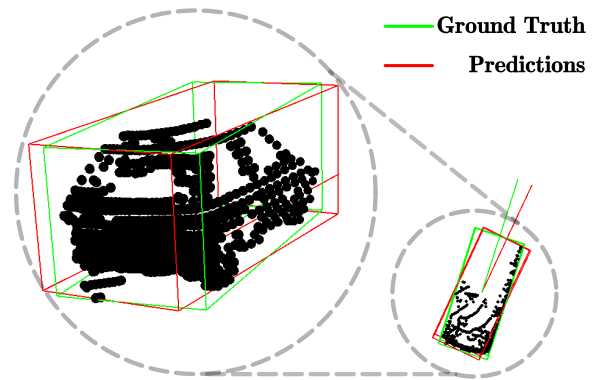


Fig. 19: Illustration of rotated overlap between a ground-truth bounding box (in green) and a detected bounding box (in red).

and cyclists, respectively) In addition, an undetected ground-truth bounding box is regarded as False Negative (FN). Note that true negative (TN) does not apply since there exist infinite possible candidates. Further, the precision P and recall R is formulated as follow:

$$P = \frac{TP}{TP + FP} = \frac{TP}{\text{all detections}} \quad (7)$$

$$R = \frac{TP}{TP + FN} = \frac{TP}{\text{all ground truths}}.$$

By plotting the Precision \times Recall Curve (PRC), the area under the curve tends to indicate the performance of a detector. In practical cases, however, zigzag-like PRC poses challenges to accurately calculate its area. As such, KITTI adopted $AP@S_N$ Metric as an alternative to circumvent the calculations directly. We presume $S = [q_0, q_0 + \frac{q_1 - q_0}{N-1}, q_0 + \frac{2(q_1 - q_0)}{N-1}, \dots, q_1]$, where we denote by S a subset of N equally spaced recall levels,

$$AP = \frac{1}{N} \sum_{r \in S} P_{\text{interpolate}}(r), \quad (8)$$

with

$$P_{\text{interpolate}}(r) = \max_{\tilde{r}: \tilde{r} \geq r} P(\tilde{r}). \quad (9)$$

Instead of taking the precision at each point into account, the previous version of KITTI benchmark performs evaluation on $AP@S_{11}$ Metric via taking the maximum precision whose recall is greater than \tilde{r} , denote by $P_{\text{interp}}(r)$, of which $S_{11} = [0, 0.1, 0.2, \dots, 1]$ is considered. It is important to note that, KITTI updates its protocol on 08.10.2019 for fairly assessing the performance of a detector via using $AP@S_{40}$ Metric [94], with 40 recall levels being evaluated, of which $S_{40} = [1/40, 2/40, 3/40, \dots, 1]$. The mean AP (mAP) can be easily obtained by averaging AP over all classes in a certain dataset, that is:

$$\text{mAP} = \frac{1}{|\mathcal{C}|} \sum_{i=1}^{|\mathcal{C}|} AP_i. \quad (10)$$

where \mathcal{C} is a subset of interested categories, AP_i denotes the AP of i -th class. Take KITTI [19, 51] for example, the Average Precision (AP) is the official KITTI evaluation protocol. Specifically, the rotated 3D IoU of 0.7, 0.5, and 0.5

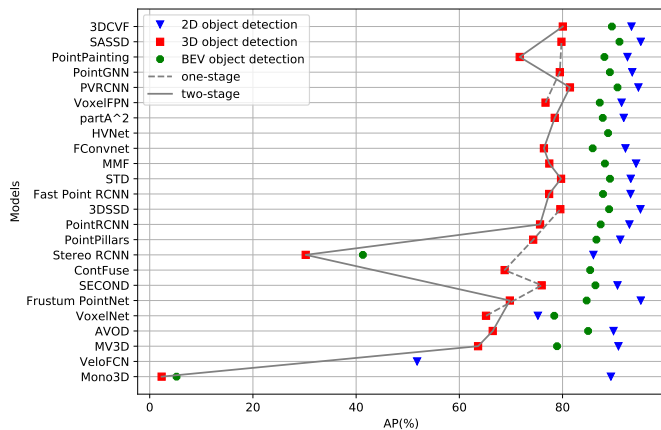


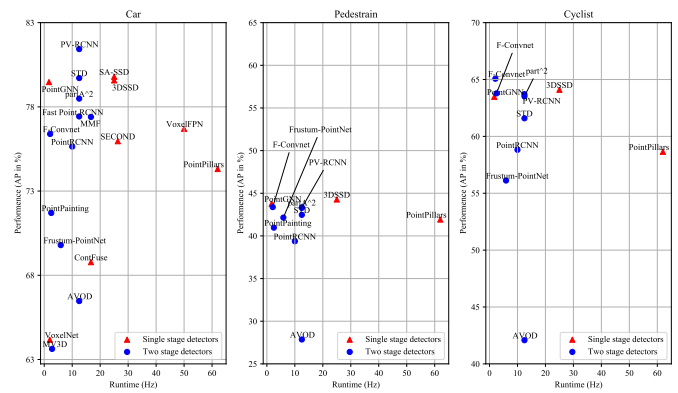
Fig. 20: The performance of *Car* category of moderate difficulty on 2D, 3D and BEV object detection for each state-of-the-art method. 2D object detection is drawn as blue triangles, BEV object detection is drawn as green circles and 3D object detection is drawn as red squares. Two-stage methods is drawn as solid lines and one-stage methods is drawn as dotted lines.

is for the categories of car, cyclist, and pedestrian respectively. Note that the performance of moderate difficulty is paramount in terms of evaluation. We refer readers to [19, 51, 93, 95] therein for more specific details.

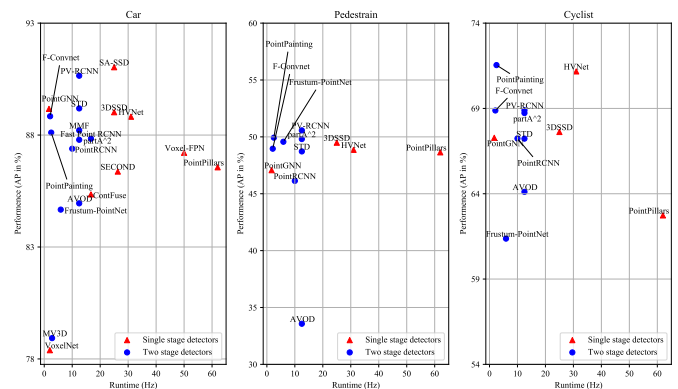
B. Comprehensive Comparison of the State-of-the-arts

In this section, we exploit a series of quantitative analysis on the basis of AP on the publicly available benchmark KITTI dataset. Table III and Table IV summarize the results of 3D object detection and bird’s eye view detection on the KITTI test server, respectively. Point cloud-based methods still predominate the benchmark at present, though multi-modal fusion-based methods are closing the gap somewhat. As forementioned above, fusing these two modalities together is non-trivial due to view misalignment. On the one hand, the monocular or stereo cameras indeed bring extra source information as a supplementary, which circumvent the risk of over-reliance on a single sensor. On the other hand, multiple sensors hinder the runtime and make it hard to deploy given the requirement of continuous synchronization. As such, trade-off exists all the time. Note that although depth ambiguity can be mitigated by 3D depth estimation, the empirical error grows quadratically as the depth increases in the context of stereo-based 3D depth estimation. Hence, the performance of image-based method is still far from satisfactory.

All along, detectors have been seeking a balance between speed and accuracy. Runtime is vital to real-time system. Fig. 21(a) and Fig. 21(b) manifest 3D detection performance and bird’s eye view performance vs runtime on KITTI test [19, 51] set. For 3D detection, PV-RCNN [23] outperforms all other methods by a large margin in terms of *Car* category. Whereas, SA-SSD [40] and 3DSSD [39] have shown a possibility of being able to trade off both speed and accuracy, especially for point-based methods, such a result is encouraging and promising. Remarkably, SA-SSD [40] still rank 1st place in



(a) 3D detection performance vs runtime in KITTI test [19, 51] set. Two-stage methods drawn as blue circles and one-stage methods drawn as red triangles. SA-SSD [40] and 3DSSD [39] are well balanced both speed and accuracy. PV-RCNN [23] outperforms all other methods by a large margin.



(b) Bird’s eye view performance vs runtime in KITTI test [19, 51] set. Two-stage methods drawn as blue circles and one-stage methods drawn as red triangles. SA-SSD [40] rank 1st place in KITTI BEV benchmark for car category currently. Both HVNet [47] and [57] have achieved the state of the art, but given the runtime, HVNet is more likely to deploy in real-time systems.

Fig. 21: Performance vs Runtime. We report AP unless otherwise noted.

KITTI BEV benchmark for *Car* category of moderate difficulty as of Apr. 17th, 2021.

Furthermore, In Fig. 20, we plotted the performance of all reviewed state-of-the-art methods in the context of 2D, 3D, and BEV object detection. Single-state methods have been closing the gap with the two stage methods ever since last year. Still, Fig. 20 reveals a disparity between 3D object detection and its counterpart, namely, 2D object detection.

Given that calculating the 11-point/40-point interpolation circumvents the estimation of area directly, we plot the precision-recall curve for more intuitive comparison of the state-of-the-art methods manifested in Section IV on the 3D/BEV detection leaderboard in Appendix VI and Appendix VII. It can be seen intuitively from the precision-recall curve, the detection performance of pedestrian and cyclist still exists a far cry from car detection. On the one hand, car category is more resilient to occlusion compared with the other two categories, on the other hand, hyper-parameters need to be fine-tuned for the specific category rather than using the same set of hyper-parameters as *Car* category.

TABLE III: Comprehensive comparison of the state-of-the-art 3D object detection AP_{3D} (in %) on KITTI test split by submitting to official test server. All these methods follow the official KITTI evaluation protocol, i.e., the rotated 3D IoU of 0.7, 0.5, and 0.5 is for the categories of *Car*, *Cyclist*, and *Pedestrian* respectively. Note that the symbol ‘-’ means the results are unavailable.

Input	Methods	Speed (fps)	Cars			Pedestrians			Cyclists		
			Easy	Moderate	Hard	Easy	Moderate	Hard	Easy	Moderate	Hard
Images	Monocular-based Methods	Deep MANTA [28]	-	-	-	-	-	-	-	-	-
		Deep3DBox [29]	-	-	-	-	-	-	-	-	-
		MF3D [30]	-	-	-	-	-	-	-	-	-
		Mono3D [27]	-	2.53	2.31	2.31	-	-	-	-	-
		GS3D [31]	-	4.47	2.9	2.47	-	-	-	-	-
		Mono3D-PLiDAR [32]	-	1.76	7.5	6.1	-	-	-	-	-
	Stereo-based Methods	3DOP [35, 55]	-	-	-	-	-	-	-	-	-
		Stereo R-CNN [33]	-	47.58	30.23	23.72	-	-	-	-	-
Point clouds	Multi-view -based Methods	VeloFCN [36]	1.0	-	-	-	-	-	-	-	-
		PIXOR [37]	28.6	-	-	-	-	-	-	-	-
	Voxel-based Methods	HVNet [47]	31	-	-	-	-	-	-	-	-
		VoxelNet [45]	2.0	77.82	64.17	57.51	-	-	-	-	-
		PointPillars [43]	62.0	82.58	74.31	68.99	51.45	41.92	38.89	77.10	58.65
		SECOND [41]	26.3	84.65	75.96	68.71	-	-	-	-	-
		Voxel-FPN [44]	50	85.48	76.70	69.44	-	-	-	-	-
		Part-A ² [24]	12.5	87.81	78.49	73.51	53.10	43.35	40.06	79.17	63.52
	Point-based Methods	PointRCNN [22]	10	86.96	75.64	70.70	47.98	39.37	36.01	74.96	58.82
		Point-GNN [25]	1.7	88.33	79.47	72.29	51.92	43.77	40.14	78.60	63.48
		3DSSD [39]	25.0	88.36	79.57	74.55	54.64	44.27	40.23	82.48	64.10
	Point-Voxel Methods	Fast Point R-CNN [63]	16.7	85.29	77.40	70.24	-	-	-	-	-
		STD [38]	12.5	87.95	79.71	75.09	53.29	42.47	38.35	78.69	61.59
		SA-SSD [40]	25.0	88.75	79.79	74.16	-	-	-	-	-
		PV-RCNN [23]	12.5	90.25	81.43	76.82	52.17	43.29	40.29	78.60	63.71
Images & Point clouds (Multimodal fusion)	Sequential fusion-based Methods	Pseudo-LiDAR [64]	-	54.53	34.05	28.25	-	-	-	-	-
		Pseudo-LiDAR++ [65]	-	61.11	42.43	36.99	-	-	-	-	-
		Pseudo-LiDAR E2E [88]	-	64.75	43.92	38.14	-	-	-	-	-
		Frustum PointNets [56]	5.9	82.19	69.79	60.59	50.53	42.15	38.08	72.27	56.12
		PointPainting [57]	2.5	82.11	71.70	67.08	50.32	40.97	37.87	77.63	63.78
		F-Convnet [46]	2.1	87.36	76.39	66.69	52.16	43.38	38.80	81.98	65.07
	Parallel fusion-based Methods	MV3D [52]	2.8	74.97	63.63	54.00	-	-	-	-	-
		AVOD [53]	12.5	76.39	66.47	60.23	36.10	27.86	25.76	57.19	42.08
		ContFuse [58]	16.7	83.68	68.78	61.67	-	-	-	-	-
		MMF [66]	12.5	88.40	77.43	70.22	-	-	-	-	-
		3D-CVF [67]	-	89.20	80.05	73.11	-	-	-	-	-

C. Emerging Datasets

With the rapid evolution in the field of autonomous driving, many top tier technology companies have open-sourced their related datasets. In fact, autonomous driving covers all aspects of scene perception. Usually, the financial, material, and human resources needed for the acquisition of data are not affordable for ordinary individuals. To a certain extent, these datasets greatly promote the research process of autonomous driving. Here, we only manifest several typical ones as representatives in relation with 3D object detection for autonomous driving.

nuScenes [84]: NuScenes dataset comprises 1000 scenes, with 23 object classes and 8 attributes being fully annotated. It is the first to collect 3D data from entire autonomous vehicle sensor kit.(e.g., 6 cameras, 1 LiDAR, 5 RADAR, GPS, IMU) The full released dataset consists 1.4M object bounding boxes approximately. As a result, it is 7x more object annotations and 100x more images than the pioneering KITTI dataset. It is gathered from Boston and Singapore where the heavy and challenging driving situations are well-known. NuScenes presented a new evaluation metric, referred to as nuScenes detection score (NDS).

Waymo open dataset [91]: Waymo dataset contains approximately 3000 driving records for a total of 16.7 hours, with each 20s long. As a whole, it contains 600,000 frames, 3x

as many scenes as the nuScenes dataset, with about 25 million 3D bounding boxes and 22 million 2D bounding boxes being annotated. In addition, Waymo open dataset diversifies itself by taking into account weather conditions, periods of day and night, downtown and suburbs, etc.

Lyft dataset [90]: The Lyft dataset is captured by 10 host cars on the roads of Palo Alto, California. Each host car has seven cameras on the roof in order to capture images of surrounding environment at different fixed view points, providing 55,000 human-labeled 3D annotations on cars, pedestrians, bicycles. Besides, each host car is also equipped with one LiDAR sensor, shooting lasers all-around to acquire exact 3D spatial geometric information.

H3D dataset [96]: The Honda Research Institute 3D Dataset (H3D) collected in San Francisco Bay Area is a large-scale 3D multi-object detection and tracking dataset for 3D scene perception. H3D consists of 160 crowded traffic scenes. 1,071,302 3D bounding box labels among 8 object classes is manually annotated.

Applloscape dataset [97]: Appllo scape is a large-scale dataset for urban areas in China collected under various lighting conditions and traffic densities. Apollo scape defines 26 object classes in the dataset, with 100K 1920 × 1080 RGB images and around 1000km trajectories for complex moving traffic agents.

TABLE IV: Comprehensive comparison of the state-of-the-art BEV object detection AP_{BEV} (in %) on KITTI test split by submitting to official test server. All these methods follow the official KITTI evaluation protocol, i.e., the rotated 3D IoU of 0.7, 0.5, and 0.5 is for the categories of *Car*, *Cyclist*, and *Pedestrian* respectively. Note that the symbol ‘-’ means the results are unavailable.

Input	Methods	Speed (fps)	Cars			Pedestrians			Cyclists			
			Easy	Moderate	Hard	Easy	Moderate	Hard	Easy	Moderate	Hard	
Images	Monocular-based Methods	Deep MANTA [28]	-	-	-	-	-	-	-	-	-	
		Deep3DBox [29]	-	-	-	-	-	-	-	-	-	
		MF3D [30]	-	-	-	-	-	-	-	-	-	
		Mono3D [27]	-	5.20	5.20	4.10	-	-	-	-	-	
		GS3D [31]	-	8.41	6.08	4.94	-	-	-	-	-	
		Mono3D-PLiDAR [32]	-	21.27	13.92	11.25	-	-	-	-	-	
	Stereo-based Methods	3DOP [35, 55]	-	-	-	-	-	-	-	-	-	
	Stereo R-CNN [33]	-	61.92	41.31	33.42	-	-	-	-	-		
Point clouds	Multi-view -based Methods	VeloFCN [36]	1.0	-	-	-	-	-	-	-	-	
		PIXOR [37]	28.6	-	-	-	-	-	-	-	-	
	Voxel-based Methods	VoxelNet [45]	2.0	87.95	78.39	71.29	-	-	-	-	-	
		SECOND [41]	26.3	91.81	86.37	81.04	-	-	-	-	-	
		PointPillars [43]	62.0	90.07	86.56	82.81	57.60	48.64	45.78	79.90	62.73	55.58
		Voxel-FPN [44]	50	92.75	87.21	79.82	-	-	-	-	-	-
		Part-A ² [24]	12.5	91.70	87.79	84.61	59.04	49.81	45.92	83.43	68.73	61.85
		HVNet [47]	31	92.83	88.82	83.38	54.84	48.86	46.33	83.97	71.17	63.65
	Point-based Methods	PointRCNN [22]	10	92.13	87.39	82.72	54.77	46.13	42.84	82.56	67.24	60.28
		3DSSD [39]	25.0	92.66	89.02	85.86	60.54	49.94	45.73	85.04	67.62	61.14
		Point-GNN [25]	1.7	93.11	89.17	83.90	55.36	47.07	44.61	81.17	67.28	59.67
	Point-Voxel Methods	Fast Point R-CNN [63]	16.7	90.87	87.84	80.52	-	-	-	-	-	-
		STD [38]	12.5	94.74	89.19	86.42	60.02	48.72	44.55	81.36	67.23	59.35
		PV-RCNN [23]	12.5	94.98	90.65	86.14	59.86	50.57	46.74	82.49	68.89	62.41
SA-SSD [40]		25.0	95.03	91.03	85.96	-	-	-	-	-	-	
Images & Point clouds (Multimodal fusion)	Sequential fusion-based Methods	Pseudo-LiDAR [64]	-	67.30	45.00	38.40	-	-	-	-	-	
		Pseudo-LiDAR++ [65]	-	78.31	58.01	51.25	-	-	-	-	-	
		Pseudo-LiDAR E2E [88]	-	79.58	58.84	52.06	-	-	-	-	-	
		Frustum PointNets [56]	5.9	91.17	84.67	74.77	57.13	49.57	45.48	77.26	61.37	53.78
		F-Convnet [46]	2.1	91.51	85.84	76.11	57.04	48.96	44.33	84.16	68.88	60.05
		PointPainting [57]	2.5	92.45	88.11	83.36	58.70	49.93	46.29	83.91	71.54	62.97
	Parallel fusion-based Methods	MV3D [52]	2.8	86.62	78.93	69.80	-	-	-	-	-	-
		AVOD [53]	12.5	89.75	84.95	78.32	42.58	33.57	30.14	64.11	48.15	42.37
		ContFuse [58]	16.7	94.07	85.35	75.88	-	-	-	-	-	-
		MMF [66]	12.5	93.67	88.21	81.99	-	-	-	-	-	-
	3D-CVF [67]	-	93.52	89.56	82.45	-	-	-	-	-	-	

Argoverse dataset [92]: Argoverse dataset contains 3D tracking annotations, with 113 scenes being manually labeled. Each scene is composed of a sequence of 15 to 30 seconds. There are more than 10,000 object tracking labels in total. Besides, Argoverse dataset extracted 324,557 interesting vehicle trajectories from over 1,000 driving hours. It is noteworthy that Argoverse is the first released dataset with high-definition (HD) maps.

Autonomous driving involves multiple subtasks such as 2D/3D object detection, semantic/instance segmentation, lane detection, depth estimation and completion, object tracking, and domain adaptation, etc. It is easier for beginners to get started with KITTI dataset, since it covers most of the tasks aforementioned, with abundant open resources in each track. In addition, nuScenes keeps up with the pace. The experiments in many papers are based on these two datasets and the subsequent ones are trying to adapt to their data structure and evaluation protocol. In terms of scale and diversity, Waymo open dataset undoubtedly dominates, however, such a huge dataset is still hostile to computing resources for academia.

D. Research Challenges and Opportunities

The future directions of 3D object detection should be elaborated based on the challenges posed in the previous reviewed literature.

- 1) First, image-based methods still exist a far cry from the state-of-the-art LiDAR-based methods due to lack of depth information, which is of great significance for accurate 3D perception. Stereo or monocular cameras are several orders of magnitude cheaper than LiDAR, with discriminative texture information being available. Besides, having a secondary sensor to fall-back onto in case of an outage can circumvent the safety risk of over-reliance on a single sensor. To this end, image-based method is still a compelling research hotspot.
- 2) Second, multimodal fusion is an increasingly popular trend. Intuitively, multimodal fusion should yield better results when more source information has been made available. Nevertheless, multimodal fusion-based methods lag behind point cloud-based at present. In fact, exploiting the synergies is non-trivial in the light of viewpoint misalignment. In addition, synchronizing and calibrating all sensors to avoid drift over time also poses a great challenge for applications of fusion-based methods. How to bring the best of two worlds together is still a tricky yet largely unexplored problem.
- 3) Third, GNNs are proposed to reason on Non-Euclidean data, its efficiency has been proved in classification and segmentation task. However, little research has looked into using GNNs for 3D object detection in the context

TABLE V: A summary of publicly available datasets for 3D object detection in the context of autonomous driving

Dataset Name	Year	Scenes	Classes	360° cameras	Size	Frames	3D Boxes	Cites
KITTI [19, 51]	2012	50	8	×	43.67(train)	15K	200K	5011
nuScenes [84]	2019	1K	23	✓	75.75(train+val)	40K	1.4M	225
Lyft L5 [90]	2019	1805	9	✓	102.34(train)	46K	1.3M	-
H3D [96]	2019	160	8	×	86.02(train+val+test)	27K	1.1M	31
ApploScape	2019	103	26	×	206.16(train)	100K	-	78
Argoverse [92]	2019	113	15	✓	97.81(train+val+test)	44K	993K	88
Waymo [91]	2020	1K	4	✓	336.62(train+val)	200K	12M	31

of autonomous driving as far as we know until Shi et al proposed Point-GNN [25].

- 4) Fourth, 3D convolution has not been the bottleneck of latency ever since Yan et al proposed SECOND [41]. As such, voxel-based methods tend to pay more attention to accuracy improvement. Simultaneously, point-based methods are exhausted with computation cost though, they could more easily capture fine-grained semantics. It is also important to note that the performance of existing point-based two stage methods drop dramatically compared with voxel-based methods [39] when faced with considerable points, e.g., nuScenes [84]. Point-voxel-based methods (e.g., PV-RCNN [23], SA-SSD [40]) are likely the one of most promising research directions at present. There still remains much to be done.
- 5) Last but not least, pseudo LiDAR indeed provides enlightenments on dealing with image data and broadens the source information. Besides, fusion of LiDAR and pseudo-LiDAR is also a new direction that is worth trying. Ultimately, adversarial attacks in 3D object detection should not be forsaken by the mainstream computer vision communities along with the continuing evolution of 3D object detection.

VI. CONCLUSION

Remarkable achievements have been made in 3D object detection over recent years. This survey extensively reviews the latest representative detectors, with close analysis of their pros and cons. Our taxonomy is based on sensor modality: monocular/stereo image-based, point cloud-based and multimodal fusion-based methods. Furthermore, we classify point cloud-based methods into multi-view-based, voxel-based, point-based, and point-voxel-based from the perspective of representation learning. We also provide commonly used metrics, evolutions of 3D object detection in the context of autonomous driving, and comprehensive comparisons of the state-of-the-arts, together with insightful observations being manifested. We hope that this survey is a stepping stone in the direction of 3D object detection and is inspiring more follow-up literature in this area.

REFERENCES

- [1] “2018 fatal motor vehicle crashes: Overview,” 2019. [Online]. Available: <https://crashstats.nhtsa.dot.gov/Api/Public/ViewPublication/812826>
- [2] “Automated vehicles for safety,” 2019. [Online]. Available: <https://www.nhtsa.gov/technology-innovation/automated-vehicles-safety>
- [3] “Self-driving cars: the impact on people with disabilities,” 2019. [Online]. Available: https://rudermanfoundation.org/white_papers/self-driving-cars-the-impact-on-people-with-disabilities/
- [4] Z. Liang, Y. Guo, Y. Feng, W. Chen, L. Qiao, L. Zhou, J. Zhang, and H. Liu, “Stereo matching using multi-level cost volume and multi-scale feature constancy,” *TPAMI*, 2019.
- [5] C. R. Qi, H. Su, K. Mo, and L. J. Guibas, “Pointnet: Deep learning on point sets for 3d classification and segmentation,” in *CVPR*, 2017.
- [6] M. M. Rahman, Y. Tan, J. Xue, and K. Lu, “Recent advances in 3d object detection in the era of deep neural networks: A survey,” *TIP*, 2019.
- [7] E. Arnold, O. Y. Al-Jarrah, M. Dianati, S. Fallah, D. Oxtoby, and A. Mouzakitis, “A survey on 3d object detection methods for autonomous driving applications,” *IEEE Transactions on Intelligent Transportation Systems*, 2019.
- [8] Y. Guo, H. Wang, Q. Hu, H. Liu, L. Liu, and M. Benamoun, “Deep learning for 3d point clouds: A survey,” *TPAMI*, 2019.
- [9] L. Jiao, F. Zhang, F. Liu, S. Yang, L. Li, Z. Feng, and R. Qu, “A survey of deep learning-based object detection,” *IEEE Access*, 2019.
- [10] Z. Zou, Z. Shi, Y. Guo, and J. Ye, “Object detection in 20 years: A survey,” *arXiv preprint arXiv:1905.05055*, 2019.
- [11] R. Girshick, “Fast r-cnn,” in *ICCV*, 2015.
- [12] K. He, X. Zhang, S. Ren, and J. Sun, “Spatial pyramid pooling in deep convolutional networks for visual recognition,” in *ECCV*, 2014.
- [13] S. Ren, K. He, R. B. Girshick, and J. Sun, “Faster R-CNN: towards real-time object detection with region proposal networks,” in *NeurIPS*, 2015.
- [14] J. Redmon, S. K. Divvala, R. B. Girshick, and A. Farhadi, “You only look once: Unified, real-time object detection,” in *CVPR*, 2016.
- [15] J. Redmon and A. Farhadi, “YOLO9000: better, faster, stronger,” *CoRR*, 2016.
- [16] W. Liu, D. Anguelov, D. Erhan, C. Szegedy, S. E. Reed, C. Fu, and A. C. Berg, “SSD: single shot multibox

- detector,” in *ECCV*, 2016.
- [17] T.-Y. Lin, P. Goyal, R. Girshick, K. He, and P. Dollár, “Focal loss for dense object detection,” in *ICCV*, 2017.
- [18] K. He, G. Gkioxari, P. Dollár, and R. B. Girshick, “Mask R-CNN,” in *ICCV*, 2017.
- [19] A. Geiger, P. Lenz, and R. Urtasun, “Are we ready for autonomous driving? the kitti vision benchmark suite,” in *CVPR*, 2012.
- [20] Y. Li, R. Bu, M. Sun, W. Wu, X. Di, and B. Chen, “Pointcnn: Convolution on x-transformed points,” in *NeurIPS*, 2018.
- [21] J. Tu, M. Ren, S. Manivasagam, M. Liang, B. Yang, R. Du, F. Cheng, and R. Urtasun, “Physically realizable adversarial examples for lidar object detection,” in *CVPR*, 2020.
- [22] S. Shi, X. Wang, and H. Li, “Pointcnn: 3d object proposal generation and detection from point cloud,” in *CVPR*, 2019.
- [23] S. Shi, C. Guo, L. Jiang, Z. Wang, J. Shi, X. Wang, and H. Li, “PV-RCNN: point-voxel feature set abstraction for 3d object detection,” *CVPR*, 2019.
- [24] S. Shi, Z. Wang, J. Shi, X. Wang, and H. Li, “From points to parts: 3d object detection from point cloud with part-aware and part-aggregation network,” 2020.
- [25] W. Shi and R. R. Rajkumar, “Point-gnn: Graph neural network for 3d object detection in a point cloud,” in *CVPR*, 2020.
- [26] D. Feng, C. Haase-Schütz, L. Rosenbaum, H. Hertlein, C. Glaeser, F. Timm, W. Wiesbeck, and K. Dietmayer, “Deep multi-modal object detection and semantic segmentation for autonomous driving: Datasets, methods, and challenges,” *IEEE Transactions on Intelligent Transportation Systems*, 2020.
- [27] X. Chen, K. Kundu, Z. Zhang, H. Ma, S. Fidler, and R. Urtasun, “Monocular 3d object detection for autonomous driving,” in *CVPR*, 2016.
- [28] F. Chabot, M. Chaouch, J. Rabarisoa, C. Teulière, and T. Chateau, “Deep MANTA: A coarse-to-fine many-task network for joint 2d and 3d vehicle analysis from monocular image,” in *CVPR*, 2017.
- [29] A. Mousavian, D. Anguelov, J. Flynn, and J. Kosecka, “3d bounding box estimation using deep learning and geometry,” in *CVPR*, 2017.
- [30] B. Xu and Z. Chen, “Multi-level fusion based 3d object detection from monocular images,” in *CVPR*, 2018.
- [31] B. Li, W. Ouyang, L. Sheng, X. Zeng, and X. Wang, “Gs3d: An efficient 3d object detection framework for autonomous driving,” in *CVPR*, 2019.
- [32] X. Weng and K. Kitani, “Monocular 3d object detection with pseudo-lidar point cloud,” in *ICCV*, 2019.
- [33] P. Li, X. Chen, and S. Shen, “Stereo r-cnn based 3d object detection for autonomous driving,” in *CVPR*, 2019.
- [34] X. Chen, K. Kundu, Y. Zhu, A. G. Berneshawi, H. Ma, S. Fidler, and R. Urtasun, “3d object proposals for accurate object class detection,” in *NeurIPS*, 2015.
- [35] X. Chen, K. Kundu, Y. Zhu, H. Ma, S. Fidler, and R. Urtasun, “3d object proposals using stereo imagery for accurate object class detection,” *TPAMI*, 2018.
- [36] B. Li, T. Zhang, and T. Xia, “Vehicle detection from 3d lidar using fully convolutional network,” in *Robotics*, 2016.
- [37] B. Yang, W. Luo, and R. Urtasun, “Pixor: Real-time 3d object detection from point clouds,” in *CVPR*, 2018.
- [38] Z. Yang, Y. Sun, S. Liu, X. Shen, and J. Jia, “Std: Sparse-to-dense 3d object detector for point cloud,” in *ICCV*, 2019.
- [39] Z. Yang, Y. Sun, S. Liu, and J. Jia, “3dssd: Point-based 3d single stage object detector,” *CVPR*, 2020.
- [40] C. He, H. Zeng, J. Huang, X.-S. Hua, and L. Zhang, “Structure aware single-stage 3d object detection from point cloud,” in *CVPR*, 2020.
- [41] Y. Yan, Y. Mao, and B. Li, “Second: Sparsely embedded convolutional detection,” *Sensors*, 2018.
- [42] Y. Zhou, P. Sun, Y. Zhang, D. Anguelov, J. Gao, T. Ouyang, J. Guo, J. Ngiam, and V. Vasudevan, “End-to-end multi-view fusion for 3d object detection in lidar point clouds,” in *Conference on Robot Learning*. PMLR, 2020.
- [43] A. H. Lang, S. Vora, H. Caesar, L. Zhou, J. Yang, and O. Beijbom, “Pointpillars: Fast encoders for object detection from point clouds,” in *CVPR*, 2019.
- [44] B. Wang, J. An, and J. Cao, “Voxel-fpn: multi-scale voxel feature aggregation in 3d object detection from point clouds,” 2019.
- [45] Y. Zhou and O. Tuzel, “Voxelnet: End-to-end learning for point cloud based 3d object detection,” in *CVPR*, 2018.
- [46] Z. Wang and K. Jia, “Frustum convnet: Sliding frustums to aggregate local point-wise features for amodal 3d object detection,” in *IROS*, 2019.
- [47] M. Ye, S. Xu, and T. Cao, “Hvnet: Hybrid voxel network for lidar based 3d object detection,” 2020.
- [48] Y. Park, S. M. Yun, C. S. Won, K. Cho, K. Um, and S. Sim, “Calibration between color camera and 3d LIDAR instruments with a polygonal planar board,” *Sensors*, 2014.
- [49] R. Ishikawa, T. Oishi, and K. Ikeuchi, “Lidar and camera calibration using motions estimated by sensor fusion odometry,” in *IROS*, 2018.
- [50] W. Lee, C. Won, and J. Lim, “Unified calibration for multi-camera multi-lidar systems using a single checkerboard,” in *IROS*, 2020.
- [51] A. Geiger, P. Lenz, C. Stiller, and R. Urtasun, “Vision meets robotics: The kitti dataset,” *The International Journal of Robotics Research*, 2013.
- [52] X. Chen, H. Ma, J. Wan, B. Li, and T. Xia, “Multi-view 3d object detection network for autonomous driving,” in *CVPR*, 2017.
- [53] J. Ku, M. Mozifian, J. Lee, A. Harakeh, and S. L. Waslander, “Joint 3d proposal generation and object detection from view aggregation,” in *IROS*, 2018.
- [54] S. Song and J. Xiao, “Deep sliding shapes for amodal 3d object detection in RGB-D images,” in *CVPR*, 2016.
- [55] X. Chen, K. Kundu, Y. Zhu, A. G. Berneshawi, H. Ma, S. Fidler, and R. Urtasun, “3d object proposals for accurate object class detection,” in *NeurIPS*, 2015.
- [56] C. R. Qi, W. Liu, C. Wu, H. Su, and L. J. Guibas,

- “Frustum pointnets for 3d object detection from rgb-d data,” in *CVPR*, 2018.
- [57] S. Vora, A. H. Lang, B. Helou, and O. Beijbom, “Point-painting: Sequential fusion for 3d object detection,” in *CVPR*, 2020.
- [58] M. Liang, B. Yang, S. Wang, and R. Urtasun, “Deep continuous fusion for multi-sensor 3d object detection,” in *ECCV*, 2018.
- [59] J. H. Hosang, R. Benenson, P. Dollár, and B. Schiele, “What makes for effective detection proposals?” *TPAMI*, 2016.
- [60] K. E. A. van de Sande, J. R. R. Uijlings, T. Gevers, and A. W. M. Smeulders, “Segmentation as selective search for object recognition,” in *ICCV*, 2011.
- [61] C. L. Zitnick and P. Dollár, “Edge boxes: Locating object proposals from edges,” in *ECCV*. Springer.
- [62] F. Moreno-Noguer, V. Lepetit, and P. Fua, “Accurate non-iterative $O(n)$ solution to the pnp problem,” in *ICCV*, 2007.
- [63] Y. Chen, S. Liu, X. Shen, and J. Jia, “Fast point R-CNN,” in *ICCV*, 2019.
- [64] Y. Wang, W.-L. Chao, D. Garg, B. Hariharan, M. Campbell, and K. Q. Weinberger, “Pseudo-lidar from visual depth estimation: Bridging the gap in 3d object detection for autonomous driving,” in *CVPR*, 2019.
- [65] Y. You, Y. Wang, W. Chao, D. Garg, G. Pleiss, B. Hariharan, M. E. Campbell, and K. Q. Weinberger, “Pseudo-lidar++: Accurate depth for 3d object detection in autonomous driving,” in *ICLR*, 2020.
- [66] M. Liang, B. Yang, Y. Chen, R. Hu, and R. Urtasun, “Multi-task multi-sensor fusion for 3d object detection,” in *CVPR*, 2019.
- [67] J. H. Yoo, Y. Kim, J. S. Kim, and J. W. Choi, “3d-cvf: Generating joint camera and lidar features using cross-view spatial feature fusion for 3d object detection,” 2020.
- [68] V. Lepetit, F. Moreno-Noguer, and P. Fua, “Epnf: An accurate $O(n)$ solution to the pnp problem,” *Int. J. Comput. Vis.*, 2009.
- [69] K. He, X. Zhang, S. Ren, and J. Sun, “Deep residual learning for image recognition,” in *CVPR*, 2016.
- [70] T. Lin, P. Dollár, R. B. Girshick, K. He, B. Hariharan, and S. J. Belongie, “Feature pyramid networks for object detection,” in *CVPR*, 2017.
- [71] H. Fu, M. Gong, C. Wang, K. Batmanghelich, and D. Tao, “Deep ordinal regression network for monocular depth estimation,” in *CVPR*, 2018.
- [72] O. Ronneberger, P. Fischer, and T. Brox, “U-net: Convolutional networks for biomedical image segmentation,” in *MICCAI*, 2015.
- [73] Z. Liu, H. Tang, Y. Lin, and S. Han, “Point-voxel CNN for efficient 3d deep learning,” in *NeurIPS*, 2019.
- [74] C. R. Qi, L. Yi, H. Su, and L. J. Guibas, “Pointnet++: Deep hierarchical feature learning on point sets in a metric space,” in *NeurIPS*, 2017.
- [75] Y. Wang, Y. Sun, Z. Liu, S. E. Sarma, M. M. Bronstein, and J. M. Solomon, “Dynamic graph cnn for learning on point clouds,” *TOG*, 2019.
- [76] L. Wang, Y. Huang, Y. Hou, S. Zhang, and J. Shan, “Graph attention convolution for point cloud semantic segmentation,” in *CVPR*, 2019.
- [77] X. Qi, R. Liao, J. Jia, S. Fidler, and R. Urtasun, “3d graph neural networks for RGBD semantic segmentation,” in *ICCV*, 2017.
- [78] T. N. Kipf and M. Welling, “Semi-supervised classification with graph convolutional networks,” in *ICLR*, 2017.
- [79] W. L. Hamilton, Z. Ying, and J. Leskovec, “Inductive representation learning on large graphs,” in *NeurIPS*, 2017.
- [80] Z. Wu, S. Pan, F. Chen, G. Long, C. Zhang, and P. S. Yu, “A comprehensive survey on graph neural networks,” 2019.
- [81] M. Feng, S. Z. Gilani, Y. Wang, L. Zhang, and A. Mian, “Relation graph network for 3d object detection in point clouds,” *TIP*, 2021.
- [82] J. Zarzar, S. Giancola, and B. Ghanem, “Pointrgcn: Graph convolution networks for 3d vehicles detection refinement,” 2019.
- [83] S. Wu, X. Li, and X. Wang, “Iou-aware single-stage object detector for accurate localization,” *arXiv preprint arXiv:1912.05992*, 2019.
- [84] H. Caesar, V. Bankiti, A. H. Lang, S. Vora, V. E. Liong, Q. Xu, A. Krishnan, Y. Pan, G. Baldan, and O. Beijbom, “nusenes: A multimodal dataset for autonomous driving,” *arXiv preprint arXiv:1903.11027*, 2019.
- [85] Y. LeCun, Y. Bengio, and G. Hinton, “Deep learning,” *nature*, 2015.
- [86] C. G. Snoek, M. Worring, and A. W. Smeulders, “Early versus late fusion in semantic video analysis,” in *ACM MM*, 2005.
- [87] J. Chang and Y. Chen, “Pyramid stereo matching network,” in *CVPR*, 2018.
- [88] R. Qian, D. Garg, Y. Wang, Y. You, S. Belongie, B. Hariharan, M. Campbell, K. Q. Weinberger, and W.-L. Chao, “End-to-end pseudo-lidar for image-based 3d object detection,” in *CVPR*, 2020.
- [89] W. Liu, D. Anguelov, D. Erhan, C. Szegedy, S. E. Reed, C. Fu, and A. C. Berg, “SSD: single shot multibox detector,” in *ECCV*, 2016.
- [90] R. Kesten, M. Usman, J. Houston, T. Pandya, K. Nadhamuni, A. Ferreira, M. Yuan, S. B. Low, A. Jain, P. Ondruska, S. Omari, S. Shah, A. Kulkarni, A. Kazakova, C. Tao, L. Platinsky, W. Jiang, and V. Shet., “Lyft level 5 av dataset 2019,” in *None*, 2019.
- [91] P. Sun, H. Kretschmar, X. Dotiwalla, A. Chouard, V. Patnaik, P. Tsui, J. Guo, Y. Zhou, Y. Chai, B. Caine, V. Vasudevan, W. Han, J. Ngiam, H. Zhao, A. Timofeev, S. Ettinger, M. Krivokon, A. Gao, A. Joshi, Y. Zhang, J. Shlens, Z. Chen, and D. Anguelov, “Scalability in perception for autonomous driving: Waymo open dataset,” in *CVPR*, 2020.
- [92] M.-F. Chang, J. W. Lambert, P. Sangkloy, J. Singh, S. Bak, A. Hartnett, D. Wang, P. Carr, S. Lucey, D. Ramanan, and J. Hays, “Argoverse: 3d tracking and forecasting with rich maps,” in *CVPR*, 2019.
- [93] M. Everingham, L. Van Gool, C. K. I. Williams, J. Winn, and A. Zisserman, “The PASCAL Visual Object Classes

Challenge 2012 (VOC2012) Results.”

- [94] A. Simonelli, S. R. Bulò, L. Porzi, M. Lopez-Antequera, and P. Kotschieder, “Disentangling monocular 3d object detection,” in *ICCV*, 2019.
- [95] R. Padilla, S. L. Netto, and E. A. B. da Silva, “A survey on performance metrics for object-detection algorithms,” in *IWSSIP*, 2020.
- [96] A. Patil, S. Malla, H. Gang, and Y.-T. Chen, “The h3d dataset for full-surround 3d multi-object detection and tracking in crowded urban scenes,” in *International Conference on Robotics and Automation*, 2019.
- [97] Y. Ma, X. Zhu, S. Zhang, R. Yang, W. Wang, and D. Manocha, “Trafficpredict: Trajectory prediction for heterogeneous traffic-agents,” in *AAAI*, 2019.
- [98] P. Hu, J. Ziglar, D. Held, and D. Ramanan, “What you see is what you get: Exploiting visibility for 3d object detection,” 2019.
- [99] D. Zhou, J. Fang, X. Song, C. Guan, J. Yin, Y. Dai, and R. Yang, “Iou loss for 2d/3d object detection,” in *3DV*, 2019.

VII. APPENDIX

We provide details omitted in the main text.

- Appendix A: Bird’s Eye of View Algorithm (Section IV of the main paper).
- Appendix B: Front View Algorithm (Section IV of the main paper).
- Appendix C: Details of the Precision-recall Curve on the 3D/BEV Detection Leaderboard (Section V of the main paper).
- Appendix D: Details of 3D Object Detection Implementation (Section III of the main paper).

A. Bird’s Eye of View Algorithm

B. Front View Algorithm

C. Precision-Recall Curve on 3D/BEV Detection Leaderboard

We also plotted the precision-recall curve for more intuitive comparison of the state-of-the-art methods manifested in Section IV on 3D detection leaderboard VI and BEV detection leaderboard VII.

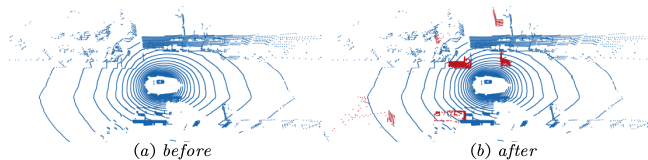


Fig. 22: (a) represents the original LiDAR point cloud. (b) shows naively “pasted” new objects (red) in the scene. Image from Hu et al. [98]

D. Implementation Details

1) Data Augmentation:

Data augmentation is indispensable during training. Augmentation methods may vary, but the “ground truth augmentor” first proposed by SECOND[41] is regarded as the gold rule adopted by most previous works. In particular, the essence

Algorithm 2 Bird’s Eye of View

Require: \mathcal{P} is a $\mathcal{N} \times 4$ matrix of point cloud data with \mathcal{N} points. Each point is denoted as (x, y, z, r) , where x, y, z is the coordinates of the point in the 3D space, r stands for the reflection intensity of LiDAR. Let $p := (p_x, p_y, p_z, p_r) \in \mathcal{P}$. Let $d \in \mathbb{N}$ be the step size for discretization, $h, w \in \mathbb{N}$ be the height and width of the desired bird’s eye image.

Ensure:

- 1: Initialize a height map H , an intensity map I and a density map D as zero matrixes with size (w, h) .
- 2: Discretize the point cloud.

$$p_x = \lfloor \frac{p_x}{d} \rfloor, \quad p_y = \lfloor \frac{p_y}{d} \rfloor.$$

- 3: Sort the points by priority of $-p_z, p_y, p_x$.
- 4: Let $\mathcal{P}^{(x,y)}$ be the set of points at (x, y) . The top point at (x, y) is:

$$top^{(x,y)} = \arg \max_{p \in \mathcal{P}^{(x,y)}} p_z.$$

- 5: Compute the values at (x, y) :

- 6: Height map

$$H_{xy} = top_z^{(x,y)};$$

Intensity map

$$I_{xy} = top_r^{(x,y)};$$

Density map

$$D_{xy} = \min\left\{1, \frac{\ln(|\mathcal{P}^{(x,y)}| + 1)}{\ln 64}\right\},$$

where $|\mathcal{P}^{(x,y)}|$ denotes the number of points in set $\mathcal{P}^{(x,y)}$.

- 7: **return** Bird’s eye view image $BEV_{w \times h \times 3}$, where $BEV(x, y) = (D_{xy}, H_{xy}, I_{xy})$.
-

Algorithm 3 Front View

Require: \mathcal{P} is a $\mathcal{N} \times 4$ matrix of point cloud data with \mathcal{N} points. Each point is denoted as (x, y, z, r) , where x, y, z are the coordinates of points in the 3D space, r stands for the reflection intensity of LiDAR. Let $p := (p_x, p_y, p_z, p_r) \in \mathcal{P}$. Denote $h, w \in \mathbb{N}$ as the height and width of the output front view image.

Ensure:

- 1: Mask the point cloud. Only preserve points within a range of interest. The masked point cloud is denoted as $\bar{\mathcal{P}}$
- 2: For every point $p \in \bar{\mathcal{P}}$:

$$p_\theta = \arctan \frac{p_y}{p_x},$$

$$p_\phi = \arctan \frac{p_z}{\sqrt{p_x^2 + p_y^2}}.$$

- 3: Let $\theta_{min}, \theta_{max}, \phi_{min}, \phi_{max}$ denote the minimum and maximum of all p_θ and p_ϕ , respectively.
- 4: Let F be a image with size (h, w) . For every point $p \in \bar{\mathcal{P}}$:

$$p_{fv_x} = (h - 1) - \left\lfloor \frac{p_\phi - \phi_{min}}{\phi_{max} - \phi_{min}} (h - 1) \right\rfloor,$$

$$p_{fv_y} = (w - 1) - \left\lfloor \frac{p_\theta - \theta_{min}}{\theta_{max} - \theta_{min}} (w - 1) \right\rfloor,$$

where $\lfloor \cdot \rfloor$ denotes a rounding operation. Then for all $p \in \bar{\mathcal{P}}$, the value of $F(p_{fv_x}, p_{fv_y})$ is

$$(p_z, \sqrt{p_x^2 + p_y^2}, p_r).$$

Pixels not specified are set as $(0, 0, 0)$.

- 5: **return** Front view image F .
-

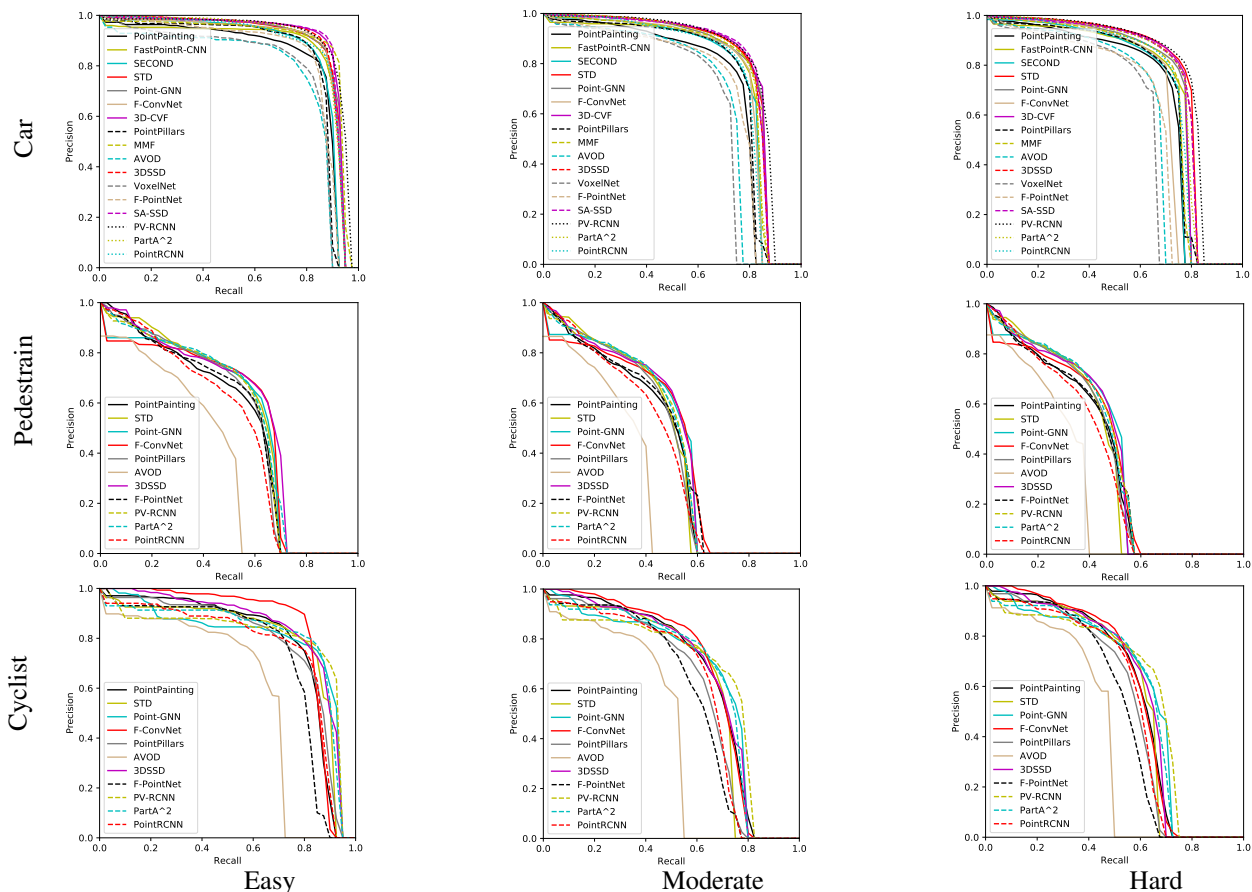


TABLE VI: Comprehensive precision-recall curve comparison of the state-of-the-art methods on the 3D detection leaderboard AP_{3D} (in %) by submitting to official test server. we plot precision-recall curve of car, pedestrian, and cyclist in terms of three difficulties, i.e. easy, moderate, and hard, respectively. Among these, the performance of moderate difficulty is the most important, especially for car category. Data from KITTI benchmark [19, 51].

of “ground truth augmentor” is to establish a ground truth database from all training sets via cropping the corresponding scenes within ground-truth boxes according to the category, then a weighted sampling is applied to randomly “copy” several ground-truth boxes from the ground truth database and “paste” them into the current scene seamlessly, as shown in Fig. 22. Since the number of objects in each frame varies, such a strategy well simulates the real complex environments. Besides, Random flipping along the x axis is also applied to each box. Global transition and rotation conformed with a uniform distribution $[-\pi/4, +\pi/4]$ are utilized to add localization noise.

2) Loss Function:

Basic loss Denote by $(x^{gt}, y^{gt}, z^{gt}, w^{gt}, l^{gt}, h^{gt}, \theta^{gt})$ ground truth box and $(x^a, y^a, z^a, w^a, l^a, h^a, \theta^a)$ its corresponding anchor. The localization regression residuals between ground truth and anchors are defined by:

$$\Delta x = \frac{x^{gt} - x^a}{d^a}, \Delta y = \frac{y^{gt} - y^a}{d^a}, \Delta z = \frac{z^{gt} - z^a}{h^a} \quad (11)$$

$$\Delta w = \log \frac{w^{gt}}{w^a}, \Delta l = \log \frac{l^{gt}}{l^a}, \Delta h = \log \frac{h^{gt}}{h^a} \quad (12)$$

$$\Delta \theta = \sin(\theta^{gt} - \theta^a), d^a = \sqrt{(w^a)^2 + (l^a)^2} \quad (13)$$

as such, the total localization loss is:

$$\mathcal{L}_{loc} = \sum_{b \in (x, y, z, w, l, h, \theta)} \text{SmoothL1}(\Delta b). \quad (14)$$

The focal loss [17] is commonly utilized to handle the class imbalance problem as,

$$\mathcal{L}_{focal}(p_t) = -\alpha_t (1 - p_t)^\gamma \log(p_t), \quad (15)$$

where p_t is the class probability of a predefined anchor.

IoU loss Since the misalignment between box quality and classification score severely affects object detection where iou denotes the 3D Intersection-over-Union (IoU) between tasks [83], many works [23, 31, 38, 99] take IoU into account to adopt quality aware loss so that the confidence predicted for each class is consistent with that of the corresponding target class:

$$q = \begin{cases} 1 & \text{if } iou > 0.75 \\ 0 & \text{if } iou < 0.25 \\ 2iou - 0.5 & \text{otherwise} \end{cases}. \quad (16)$$

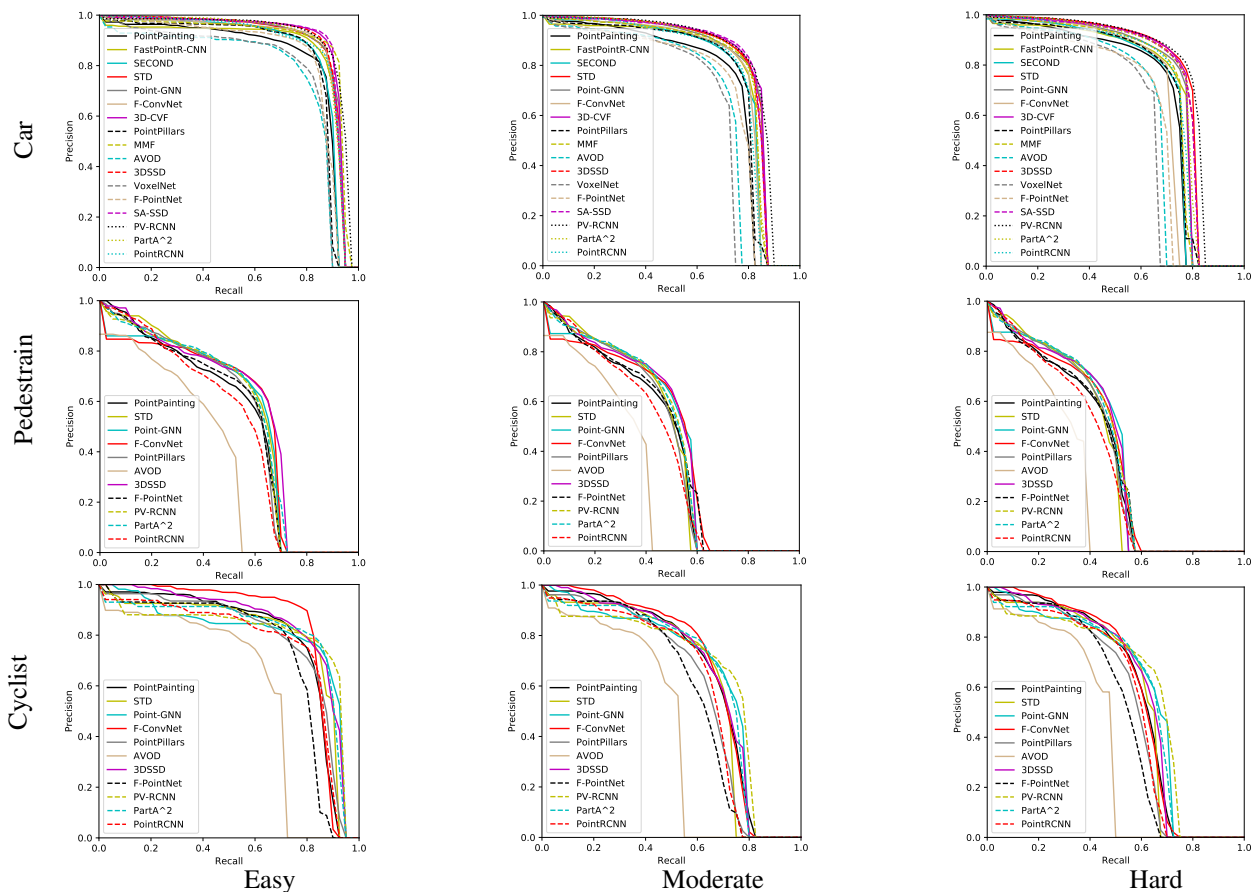


TABLE VII: Comprehensive precision-recall curve comparison of the state-of-the-art methods on the BEV detection leaderboard AP_{BEV} (in %) by submitting to official test server. we plot precision-recall curve of car, pedestrian, and cyclist in terms of three difficulties, i.e., easy, moderate, and hard, respectively. Among these, the performance of moderate difficulty is the most important, especially for *Car* category. Data from KITTI benchmark[19, 51].

ground-truth boxes and their corresponding 3D RoIs:

$$\mathcal{L}_{iou} = -[q \log(p) + (1 - q) \log(1 - p)], \quad (17)$$

where p is the predicted score, and thus, the total loss is summarized as :

$$\mathcal{L} = \frac{1}{N_{pos}} (\beta_{loc} \mathcal{L}_{loc} + \beta_{iou} \mathcal{L}_{iou}). \quad (18)$$

Corner loss Corner loss minimizes the differences between the predicted 8 corners and assigned groundtruth [38, 56], denoted by:

$$\mathcal{L}_{corner} = \sum_{k=1}^8 \|P_k - G_k\|. \quad (19)$$

Bin-based loss As shown in Fig. 23, the region along x -axis and z -axis of each interest point is discretized into a series of bins. By transforming the original regression task into bin classification and a small residual regression, the complexity of direct regression is dramatically mitigated, especially in terms of the angle regression[22, 29, 30, 46].

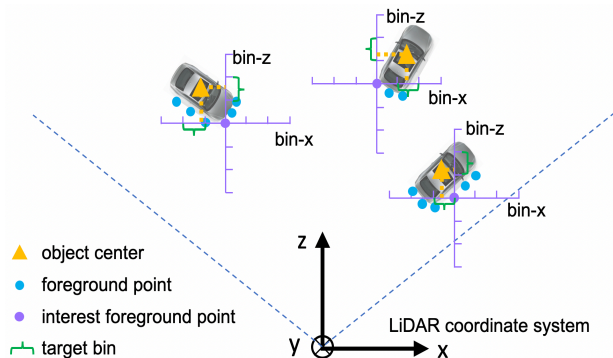


Fig. 23: Illustration of bin-based localization. The original regression problem is simply transformed into a series of discrete bin classification and residual regression. Image from Shi et al. [98]